

**SAGE III Algorithm Theoretical Basis Document (ATBD)
Chlorine Dioxide Data Products**



Compiled by the SAGE III ATBD Team

**LaRC 475-00-105
Version 1.2
18 February 2000**

TABLE OF CONTENTS

1.0 INTRODUCTION.....	1
1.1 PURPOSE.....	1
1.2 SCOPE.....	1
1.3 APPLICABLE DOCUMENTS	2
1.3.2 SAGE III ATDB Reference Documents.....	2
1.4 REVISION HISTORY	2
1.5 CONTRIBUTING AUTHORS.....	3
1.6 SAGE III STANDARD DATA PRODUCTS.....	4
PRODUCT NAME.....	4
ACCURACY.....	4
2.0 BACKGROUND.....	5
2.1 EXPERIMENTAL OBJECTIVES.....	5
2.2 RELEVANCE OF OCLO MEASUREMENTS TO EOS.....	6
3.0 ALGORITHM DESCRIPTION.....	18
3.1 INTRODUCTION.....	18
3.1.1 Physical Description.....	18
3.1.2 The Forward Problem.....	21
3.2 RETRIEVAL ALGORITHM DESCRIPTION	22
3.2.1 Overview and Assumptions.....	22
3.2.2 Species Separation Algorithm.....	24
3.2.3 Differential Retrievals of Gases (Solar and Lunar).....	31
3.3 ALGORITHM TESTING REQUIREMENTS	38
3.4 VALIDATION PLAN	38
3.5 QUALITY CONTROL AND DIAGNOSTICS	39
4.0 REFERENCES.....	40
APPENDIX A. SAGE III INSTRUMENT DESCRIPTION.....	47
APPENDIX B. IMPLIMENTATION OF ATMOSPHERIC RETRIEVALS.....	53
APPENDIX C. ATMOSPHERIC INHOMOGENEITY.....	56
APPENDIX D. MOLECULAR ABSORPTION CROSS-SECTIONS: SPECTROSCOPIC CONSIDERATIONS FOR SAGE III.....	59
D.1 INTRODUCTION	59
D.2 SPECIES SPECIFIC INFORMATION	59
D.2.1 Ozone.....	59
D.2.2 Nitrogen Dioxide.....	63
D.2.3 Oxygen.....	66
D.2.4 Water Vapor.....	67
D.2.5 The Nitrate Free Radical NO ₃	69
D.2.6 Symmetric Chlorine Dioxide OCLO.....	71
APPENDIX E. LUNAR ALTITUDE REGISTRATION.....	73

1.0 Introduction

The Stratospheric Aerosol and Gas Experiment III (SAGE III) is a critical part of the Earth Observing System (EOS). The EOS mission is to develop an understanding of the total Earth system and the effects of natural and human-induced changes on the global environment. SAGE III provides limb occultation measurements with a flexible instrument design that permits on orbit reprogramming and channel selection with up to 800 channels spanning the ultraviolet, visible, and near infrared (280-1040 nm). Solar observations will provide high resolution vertical profiles of multi-wavelength aerosol extinction, the molecular density of ozone, nitrogen dioxide, and water vapor, as well as profiles of temperature, pressure, and cloud presence. In addition, the inclusion of a repositionable solar attenuator will allow lunar occultation observations that will improve the geographic coverage and permit measurements of nitrogen trioxide and chlorine dioxide in addition to ozone, nitrogen dioxide, water vapor, and pressure.

1.1 Purpose

This Algorithm Theoretical Basis Document (ATBD) describes the algorithms used to retrieve the SAGE III chlorine dioxide data products. All SAGE III data products will be archived at the NASA Langley Research Center Distributed Active Archive Center (DAAC). This document identifies sources of input data which are required for the retrieval; provides the physical theory and mathematical background underlying the use of this information in the retrievals; describes practical considerations affecting algorithm development; and outlines a test and validation approach. However, since the retrieval of each data product depends on the form and quality of the transmission measurements (Level 1B data products) and influences other data retrievals, an overall description of the entire retrieval process is described at a high-level in Chapter 3.

1.2 Scope

An individual document has been developed for each SAGE III standard data product summarized in Table 1.2.1. This document covers the algorithm theoretical basis for the parameters to be included in the SAGE III Data Products at or near launch time. Only parameters that are to be routinely retrieved are discussed. Current development and prototyping efforts may result in modifications to parts of certain algorithms. Only the algorithms which are implemented for routine processing of SAGE III data will be preserved in the a release of this document.

1.3 Applicable Documents

1.3.1 Controlling Documents

Mission to Planet Earth Strategic Enterprise Plan 1996-2002, NASA HQ EOS, May 1996.
Execution Phase Project Plan for Earth Observing System (EOS), GSFC 170-01-01, Rev. A., May 1995.

1.3.2 SAGE III ATDB Reference Documents

SAGE III Algorithm Theoretical Basis Document: Transmission Data Products, LaRC 475-00-108, February 2000.

SAGE III Algorithm Theoretical Basis Document: Temperature and Pressure Data Products, LaRC 475-00-104, February 2000.

SAGE III Algorithm Theoretical Basis Document: Aerosol Data Products, 475-00-105, February 2000.

SAGE III Algorithm Theoretical Basis Document: Nitrogen Dioxide Data Products, LaRC 475-00-101, February 2000.

SAGE III Algorithm Theoretical Basis Document: Nitrogen Trioxide Data Products, LaRC 475-00-102, February 2000.

SAGE III Algorithm Theoretical Basis Document: Chlorine Dioxide Data Products, LaRC 475-00-103, February 2000.

SAGE III Algorithm Theoretical Basis Document: Water Vapor Data Products, LaRC 475-00-100, February 2000.

SAGE III Algorithm Theoretical Basis Document: Cloud Presence Data Products, LaRC 475-00-106, February 2000.

SAGE III Algorithm Theoretical Basis Document: Ozone Data Products, LaRC 475-00-107, February 2000.

1.4 Revision History

The original version of this document was dated November 15, 1996. Version 1.1 was released on 15 April 1997. This release, version 1.2, is dated 18 February 2000.

1.5 Contributing Authors

Each of the SAGE III ATBDs was drafted by a team of SAGE III science team members and SAGE III science cadre, led by one of the science team members. The entire team participated in oral and written revisions of the methodology and documentation as part of the SAGE III science team meetings and research activities.

Contributing Authors	Affiliation
Er-Woon Chiou	SAIC
William P. Chu, Associate PI	NASA Langley Research Center
Albert A. Chernikov	Central Aerological Observatory
Derek M. Cunnold	Georgia Tech
John DeLuise	NOAA
Philip A. Durkee	Naval Postgraduate School
Nikolai F. Elansky	Russian Academy of Science
Benjamin M. Herman	University of Arizona
Peter V. Hobbs	University of Washington
Geoff S. Kent	Science and Technology Corporation
Jacqueline Lenoble	University de Lille, France
M. P. McCormick, Principal Investigator	Hampton University
Hope A. Michelesen*	AER, Inc.
Alvin J. Miller	NOAA/NCEPS
Volker Mohnen	State University of New York at Albany
Randy Moore*	SAIC
Michael Pitts	NASA Langley Research Center
Lamont R. Poole	NASA Langley Research Center
Venkatachalam Ramaswamy	Princeton University
David Rind	Goddard Institute for Space Studies
David Risley*	SAIC
Michael W. Rowland	SAIC
Philip B. Russell	NASA Ames Research Center
Vinod K. Saxena	North Carolina State University
Eric P. Shettle	Naval Research Laboratory
Larry W. Thomson	NASA Langley Research Center
Charles R. Trepte	NASA Langley Research Center
Gabor Vali	University of Wyoming
Lelia B. Vann	NASA Langley Research Center
Pi-Huan Wang	Science and Technology Corporation
Steven C. Wofsy*	Harvard University
David C. Woods	NASA Langley Research Center
Joseph M. Zawodny*	NASA Langley Research Center

Technical assistance was provided by Susan Walters and Jackie Bumgartner.

*Lead Authors

1.6 SAGE III Standard Data Products

Table 1.2.1 SAGE III Standard Data Products

PRODUCT NAME	ACCURACY Absolute :: Relative	TEMPORAL RESOLUTION	HORIZONTAL Resolution :: Coverage	VERTICAL Resolution :: Coverage
Level 1B Transmission (≤ 80 wavelengths) Solar Events	0.05% :: 0.05%	1/(2 minutes), 30/day	<2 x <1 deg :: Global	0.5 km :: 0-100 km
Aerosol Extinction Strat. Optical Depth (at 9 wavelengths), Aerosol to molecular/extinction ratio at 1020 nm (solar only)	5% :: 5%	1/(2 minutes), 30/day	<2 x <1 deg :: Global	0.5 km :: 0-40 km
H ₂ O Concentration (Alt.) Mixing Ratio (Pressure)	10% :: 15%	1/(2 minutes), 30/day	<2 x <1 deg :: Global	0.5 km :: 0-50 km 24 levels/decade :: 1000-0.8 hPa
NO ₂ Concentration (Alt.) Mixing Ratio (Pressure) Slant Path Col. Amt. (Alt.)	10% :: 15%	1/(2 minutes), 30/day	<2 x <1 deg :: Global	0.5 km :: 10-50 km 24 levels/decade :: 250-0.8 hPa 0.5 km :: 10-50 km
NO ₃ (Lunar Only) Concentration (Alt.) Mixing Ratio (Pressure)	10% :: 10%	1/(2 minutes), ≤ 30 /day	<2 x <1 deg :: Global	0.5 km :: 20-55 km 24 levels/decade :: 50-0.4 hPa
O ₃ Concentration (Alt.) Mixing Ratio (Pressure) Slant Path Col. Amt. (Alt.)	6% :: 5%	1/(2 minutes), 30/day	<2 x <1 deg :: Global	0.5 km :: 6-85 km 24 levels/decade :: 500-0.004 hPa 0.5 km :: 50-85 km
OCIO (Lunar Only) Concentration (Alt.) Mixing Ratio (Pressure)	25% :: 20%	1/(2 minutes), ≤ 30 /day	<2 x <1 deg :: Global	0.5 km :: 15-25 km 24 levels/decade :: 121-25 hPa
Pressure	2% :: 2%	1/(2 minutes), 30/day	<2 x <1 deg :: Global	0.5 km :: 0-85 km
Temperature Profile	2K :: 2K	1/(2 minutes), 30/day	<2 x <1 deg :: Global	0.5 km :: 0-85 km 24 levels/decade :: 1000-0.004 hPa
Cloud Presence	N/A	1/(2 minutes), 30/day	<2 x <1 deg :: Global	0.5 km :: 6-30 km

2.0 Background

SAGE III is the fifth generation of solar occultation instruments designed to measure atmospheric aerosols and gaseous species in the atmosphere. The solar occultation method employs the attenuation of the Sun's rays as observed through the limb of the Earth's atmosphere to determine the vertical distribution of important atmospheric constituents. Measurements are made during each sunrise and sunset (an "event") encountered by the spacecraft (~30/day). This method is well-suited for long-term monitoring of trends and variability in key species such as ozone since the instrument is recalibrated during each event. The instrument concept originated as a hand-held, single wavelength sunphotometer (Stratospheric Aerosol Measurement or SAM) which was flown onboard an Apollo mission in 1975 (Pepin and McCormick, 1976). SAM II was a one wavelength (1000 nm) instrument which operated on Nimbus-7 between 1978 and 1994 (McCormick et al., 1979, 1981). The Stratospheric Aerosol and Gas Experiment (SAGE) operated on the Application Explorer Mission 2 (AEM-2) spacecraft between 1979 and 1981. This instrument made measurements at 4 wavelengths and measured molecular density profiles of O₃ and NO₂ in addition to aerosol extinction at 2 wavelengths (450 and 1000 nm) (McCormick et al., 1979). SAGE II has operated on the Earth Radiation Budget Satellite (ERBS) since 1984 and makes measurements at 7 wavelengths. In addition to the species measured by SAGE, SAGE II measures the molecular density profile of H₂O and aerosol extinction at 4 wavelengths (385, 453, 525 and 1020 nm) (Mauldin, 1985 McCormick, 1987). In SAGE III, a charged coupled device (CCD) linear array provides spectral coverage from 280 to 1040 nm. In addition, a single photodiode adds aerosol extinction measurements at 1550 nm. (McCormick et al., 1991; Mauldin et al., 1989; McCormick et al., 1993). A repositionable solar attenuator will permit both solar and lunar occultation measurements, increasing the geographical coverage and allowing for the detection of nitrogen trioxide and chlorine dioxide. The incorporation of the CCD array will permit the measurement of gaseous species from multichannel absorption signatures simplifying the retrieval process, and 16-bit digitization will improve the precision and altitude range of the measurements.

2.1 Experimental Objectives

The science objectives to be accomplished by SAGE III are:

- Retrieve global profiles of atmospheric aerosol extinction, temperature, and pressure and molecular density profiles of ozone, water vapor, nitrogen dioxide, nitrogen trioxide, and chlorine dioxide with 0.5 km vertical resolution;
- Characterize tropospheric as well as stratospheric clouds and investigate their effects on the Earth's environment, including radiative, microphysical, and chemical interactions;

- Determine long-term trends in gaseous species and temperature;
- Provide atmospheric data essential for the interpretation and calibration of other satellite sensors, including EOS instruments.
- Investigate the spatial and temporal variability of these species in order to determine their role in climate processes, biogeochemical cycles, and the hydrological cycle.

2.2 Relevance of OCIO Measurements to EOS

This document describes the algorithms to be developed for retrievals of OCIO, which will be measured during lunar occultations. The following section outlines the scientific background and objectives for these measurements.

Chemistry of OCIO in the Stratosphere

The major source of OCIO in the stratosphere is thought to be from the reaction



which occurs at a significant rate only when concentrations of ClO are high [McElroy *et al.*, 1986; Rodriguez *et al.*, 1986; Solomon *et al.*, 1987; Tung *et al.*, 1986]. Photolysis removes OCIO rapidly during the daytime; hence the highest concentrations occur at night. Concentrations of ClO high enough to produce observable levels of OCIO may be produced when temperatures drop below about 200 K, promoting conversion of HCl and ClNO₃ to ClOx radicals on surfaces of PSCs or on supercooled sulfate aerosol particles [Hanson and Ravishankara, 1994; Hanson *et al.*, 1994; Molina *et al.*, 1987; Solomon *et al.*, 1986]. These conditions are commonly met only in the polar regions during winter and early spring. Significant concentrations of OCIO are consequently expected to be confined to the winter polar vortices in darkness [McElroy *et al.*, 1986; Rodriguez *et al.*, 1986; Salawitch *et al.*, 1988; Solomon *et al.*, 1987; Tung *et al.*, 1986].

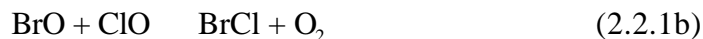
Other sources of stratospheric OCIO include [DeMore *et al.*, 1994]



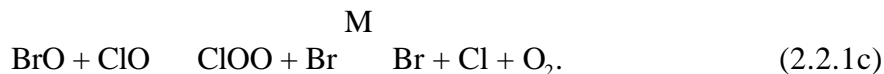
Since the rates for reactions (2.2.2)-(2.2.4) are generally slower than that for (2.2.1a), the contributions from these reactions to OCIO abundances are expected to be minor [Salawitch *et al.*, 1988]. If chlorine species have been converted to ClOx, and the air is subsequently warmed above 205 K, thermal dissociation of ClO dimer may maintain significant

concentrations of ClO in the dark, and the abundance of OCIO may increase gradually during the night from reactions (2.2.2)-(2.2.4) (see Figure 2.2.1).

The abundance of OCIO is controlled by the concentration of BrO and by the partitioning of reaction (2.2.1) into the OCIO product channel, which competes with [Friedl and Sander, 1989; Sander and Friedl, 1989; Toohey and Anderson, 1988; Turnipseed *et al.*, 1991]



and



At stratospheric temperatures the branching ratios have been measured to be approximately 0.6 for channel (1a) and 0.08 for channel (1b) [Friedl and Sander, 1989; Sander and Friedl, 1989; Turnipseed *et al.*, 1991]. Since formation of BrCl terminates bromine radical chemistry at night, the highest concentration of OCIO that can be produced by (1) is approximately 12 times (i.e., $1/0.08$) the daytime concentration of BrO. The actual concentration of OCIO depends on competition between (1) and formation of BrNO₃ via $\text{BrO} + \text{NO}_2 \rightarrow \text{BrNO}_3$. In practice concentrations of OCIO at night increase abruptly as soon as polar processes generate concentrations of ClO in excess of those of NO₃, and OCIO levels decline sharply when this process is reversed (typically in spring in the Arctic or when the vortex breaks up in the Antarctic).

Impact of OCIO on O₃ Depletion

Photochemical reactions involving production of OCIO during the daylight hours may influence the loss of O₃ in the Antarctic, but the magnitude of the contribution to O₃ depletion remains controversial [Vaida and Simon, 1995]. Channels (2.2.1b) and (2.2.1c) yield the same products; in daylight BrCl is rapidly photolyzed to Br and Cl, and ClOO is thermally decomposed to Cl and O₂. In either case O₂ is produced resulting in the net destruction of O₃ via the catalytic cycle [McElroy *et al.*, 1986]



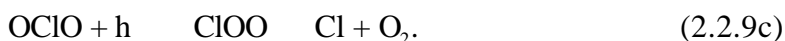
If, however, channel (2.2.1a) is accessed instead of channels (2.2.1b) and (2.2.1c), the rate of O₃ destruction is reduced since reaction (2.2.7) in the above catalytic cycle can be replaced by





For this case production and destruction of OCIO does not result in ozone loss [Vaida and Simon, 1995].

An alternate pathway for OCIO photolysis involves either direct production of O_2 or production of O_2 via the ClOO intermediate [Baumert *et al.*, 1993; Bishenden and Donaldson, 1993; Davis and Lee, 1992; Rühl *et al.*, 1990; Vaida and Simon, 1995; Vaida *et al.*, 1989], i.e.,



The result of reaction (2.2.1a) followed by either of routes (2.2.9b) or (2.2.9c) is equivalent to mechanism (2.2.7), which leads to O_3 destruction. Vaida and Simon [1995] have pointed out that, although (2.2.9b) and (2.2.9c) are not the primary photolysis channels for OCIO, a branching ratio of 0.1 to $\text{Cl} + \text{O}_2$ would lead to a predicted loss of ~3% of Antarctic O_3 . Laboratory measurements of the branching ratio have yielded widely varying results (between 0.15 [Bishenden and Donaldson, 1993] and $<5 \times 10^{-4}$ [Lawrence *et al.*, 1990]). Several studies have indicated that the branching ratio is mode specific; excitation of the bending mode in the excited electronic state favors (2.2.9b) [Davis and Lee, 1992] whereas excitation of the asymmetric stretching mode is more likely to lead to (2.2.9a) [Bishenden and Donaldson, 1993; Gole, 1980; Jafri *et al.*, 1985; Peterson and Werner, 1992; Richard and Vaida, 1991]. These results suggest that the branching ratio should be wavelength dependent.

The major products from the photolysis of OCIO in aqueous sulfuric acid solutions are ClO and O, as in the gas phase photolysis. The branching ratio for (2.2.9a) has been measured to be 0.9 [Dunn and Simon, 1992]. Cl and O_2 , produced predominantly via (2.2.9c), have also been identified [Dunn *et al.*, 1993; Dunn *et al.*, 1995]. In contrast to the homogeneous phase cases, the branching ratio for production of O_2 from photolysis of thin films of OCIO is large, 0.8 ± 0.1 [Lanzendorf and Kummel, 1996]. Upon photolysis on ice surfaces OCIO has been shown to be converted to ClOO [Pursell *et al.*, 1995]. Although the adsorption probability of OCIO on ice has been measured to be near unity [Graham *et al.*, 1996], extrapolation of the measured adsorption/desorption kinetics to polar stratospheric conditions indicates that the surface coverage will not be large enough to cause significant perturbations to the partitioning of OCIO photodecomposition products [Brown *et al.*, 1996]. Surface reactions with other species, e.g., ClNO_3 , or adsorption and subsequent decomposition on sulfate aerosol surfaces, however, may lead to significant perturbations to the partitioning of inorganic chlorine [Brown *et al.*, 1996].

History of Stratospheric Measurements

Vertical column measurements of OCIO from the ground and from the DC-8 aircraft have shown that significant concentrations are observable in both the Arctic [Perner *et al.*, 1991; Schiller *et al.*, 1990; Solomon *et al.*, 1988] and Antarctic stratosphere [Sanders *et al.*, 1989; Sanders *et al.*, 1993; Solomon *et al.*, 1987; Solomon and Sanders, 1990; Solomon *et al.*, 1989; Wahner *et al.*, 1989; Kreher *et al.*, 1996] during winter and early spring. Nighttime column abundances have been observed to reach $2\text{--}10 \times 10^{13} \text{ cm}^{-2}$ in the Arctic [Schiller *et al.*, 1990; Solomon *et al.*, 1988] and $2\text{--}16 \times 10^{13} \text{ cm}^{-2}$ in the Antarctic [Sanders *et al.*, 1989; Sanders *et al.*, 1993; Solomon *et al.*, 1987; Solomon *et al.*, 1989; Wahner *et al.*, 1989]. Twilight ($\text{SZA} < 93^\circ$) values are reduced by approximately an order of magnitude from nighttime values [Perner *et al.*, 1991; Sanders *et al.*, 1989; Schiller *et al.*, 1990; Solomon *et al.*, 1987]. Nighttime measurements in the northern midlatitudes have yielded an upper limit of $3 \times 10^{13} \text{ cm}^{-2}$ [Solomon *et al.*, 1987].

Measured abundances of OCIO appear to be negatively correlated with temperature [Sanders *et al.*, 1993; Solomon *et al.*, 1987] and abundances of NO_2 [Sanders *et al.*, 1989; Sanders *et al.*, 1993; Schiller *et al.*, 1990; Solomon *et al.*, 1988; Solomon *et al.*, 1987], HCl [Kreher *et al.*, 1996], and ClNO_3 [Sanders *et al.*, 1989] and positively correlated with abundances of BrO [Schiller *et al.*, 1990; Solomon *et al.*, 1989] and ClO [Schiller *et al.*, 1990]. These observations are consistent with the mechanisms for photochemical production and loss described above. Production of OCIO via reaction (1a) requires high concentrations of BrO and ClO . Lower temperatures are associated with higher rates of reactions of HCl , ClNO_3 [Hanson and Ravishankara, 1994; Hanson *et al.*, 1994], and BrNO_3 [Hanson and Ravishankara, 1993; Hanson and Ravishankara, 1995] on aerosol and PSC particles, leading to increased concentrations of ClO and BrO . NO_2 performs the reverse role to that of surface reactions, combining with ClO and BrO to form ClNO_3 and BrNO_3 and reducing reactants available for OCIO formation. The observed diurnal variations of OCIO are also consistent with this mechanism; as noted above, concentrations tend to be lower during twilight than during polar night since OCIO is readily photolyzed. Furthermore, the abundance of OCIO has been reported to be lower during the morning twilight than during the evening twilight [Perner *et al.*, 1991; Sanders *et al.*, 1989; Solomon and Sanders, 1990; Solomon *et al.*, 1989], which has been attributed to slow morning photolysis of a nighttime reservoir for BrO , such as BrNO_3 [Solomon *et al.*, 1989].

Model studies of OCIO Abundance

Photochemical models have been used to make quantitative comparisons of measured values of OCIO with values expected based on measured column abundances of BrO , ClO , and NO_2 [Jones *et al.*, 1989; Solomon and Sanders, 1990; Solomon *et al.*, 1989; Wahner and Schiller, 1992]. General trends have been shown to be reproducible with exceptions attributed to variations in vortex structure related to transport processes and a weakness in the present understanding of bromine chemistry [Wahner and Schiller, 1992]. The diurnal variation of OCIO has also been reproduced in model calculations [Rodriguez *et al.*, 1986; Salawitch *et al.*, 1988; Solomon *et al.*, 1989; Wahner and Schiller, 1992]. These

calculations, however, tend to overestimate OCIO abundances in the morning twilight. The discrepancy is possibly due to the formation of reservoir species from ClO and BrO via chemical pathways not currently understood [Solomon and Sanders, 1990; Solomon *et al.*, 1989].

Model calculations based on observations of OCIO, ClO, BrO, and NO₂ abundances suggest that the reaction of ClO with BrO is responsible for ~10-20% of the ozone loss observed in the Antarctic winter [Anderson *et al.*, 1989; Barrett *et al.*, 1988; Jones *et al.*, 1989; Salawitch *et al.*, 1988; Sander *et al.*, 1989; Solomon and Sanders, 1990] and a higher fraction in the Arctic. Approximately 70% of Antarctic loss has been attributed to formation of the ClO dimer via the following catalytic cycle [Jones *et al.*, 1989; Sander *et al.*, 1989; Solomon and Sanders, 1990]:



net result: $2\text{O}_3 \rightarrow 3\text{O}_2$ same as (2.2.8).

Scientific Questions

SAGE III data, consisting of lunar and solar occultations of OCIO, NO₂, NO₃, H₂O, aerosols, and O₃, can address an important set of scientific questions, which includes

1. What controls the onset of polar chemistry, defined as production of very high concentrations of halogen oxide radicals (ClO_x and BrO_x)? Is there a critical temperature? Is PSC formation required?
2. Does removal of NO_x precede conversion of HCl to ClO_x?
3. What controls the rate for regeneration of NO_x in the spring, the key limiting process for polar ozone loss?

Experimental Objectives for SAGE III

We can distinguish three phases of polar ozone and halogen chemistry:

Phase I. The onset of polar halogen chemistry begins with depletion of NO_x, caused by increasing rates for heterogeneous reactions as temperatures drop. Concentrations of ClO_x and BrO_x increase as formation of ClNO₃ and BrNO₃ is inhibited by lack of NO_x, and as HCl is converted to ClO_x by heterogeneous reactions.

Phase II. During the polar night, some fraction of NO_y is lost by formation and sedimentation of large particles containing HNO_3 .

Phase III. When the Sun returns to the polar region in the spring, rapid ozone loss occurs in the Antarctic, but return of NO_x to the system (by photolysis of HNO_3) inhibits and eventually terminates ozone destruction.

At the beginning of phase I, *SAGE III* will observe high concentrations of NO_2 and NO_3 at night in lunar occultation mode, with NO_2 gradually decreasing and NO_3 increasing over the course of the night. Concentrations of OCIO will be below observational thresholds. As phase I proceeds, levels of NO_2 and NO_3 will decline, possibly in confined altitude ranges, and, when they decline below a key level, OCIO will appear. *SAGE III* will make observations of OCIO profiles in lunar mode. The reverse evolution may occur in the spring, especially in the Arctic. As the Sun returns to the polar region, *SAGE III* may be able to make twilight solar observations in lunar mode, i.e., with reduced resolution but with a larger number of channels.

These processes have never been observed in detail because of a lack of a suitable platform. *SAGE III* provides an excellent tool to examine phase I and possibly III and to address the scientific questions by observing nocturnal vertical profiles of aerosols (including PSCs), OCIO, NO_2 , and NO_3 .

During phases II and III *SAGE III* observations of O_3 and OCIO will define rates of O_3 loss and relate O_3 losses directly to halogen radical levels. The measurements should help to define the relative rates of removal due to Br-radicals (precursors of OCIO) versus other processes.

Model simulations shown in Figures 2.2.1 and 2.2.2 provide a guide to algorithm development to address these issues. Figures 2.2.1a and 2.2.1b show diurnal variations of key species at 66 S in midwinter for air assumed to have undergone polar processing with 15% of HCl converted to ClO_x and 90% of NO_x converted to HNO_3 . The calculation was performed for an altitude of 20 km, and temperature of 198 K, and the model was allowed to march in time for 5 days after last contact with PSCs. No denitrification was assumed; hence the abundance of ClNO_3 is seen to be increasing slowly. Concentrations of OCIO reach maximum values at night equivalent to about 9 times the midday concentration of BrO. All the BrO initially present is converted to BrCl at night. Figure 2.2.1c and 2.2.1d show the identical air parcel, assumed to have never been processed by polar heterogeneous chemical reactions. Concentrations of OCIO are about one-half of the concentration in processed air, although much higher than would be found at midlatitudes because of higher ClO and lower NO_x in the midwinter, subpolar atmosphere due to low temperatures and low light levels. About one-half of the BrO present at noon is converted to BrNO_3 instead of OCIO at night.

Figure 2.2.2 shows calculations of OCIO and related species as functions of temperature, at midnight (2.2.2(a-k)) and at noon (2.2.2(l)) at 66 S latitude. The strong temperature

dependence of heterogeneous reactions converting HCl and ClONO_2 to ClO_x leads to increasing concentrations of ClO and OCIO when temperatures fall below about 203 K. The figure shows that OCIO concentrations exceeding $1 \times 10^8 \text{ cm}^{-3}$ appear abruptly when temperatures drop below 200 K, coincident with the appearance of significant quantities of ClO -dimer and HOCl . Thus SAGE III observations of OCIO will provide a direct quantitative indicator for chemical losses of polar ozone

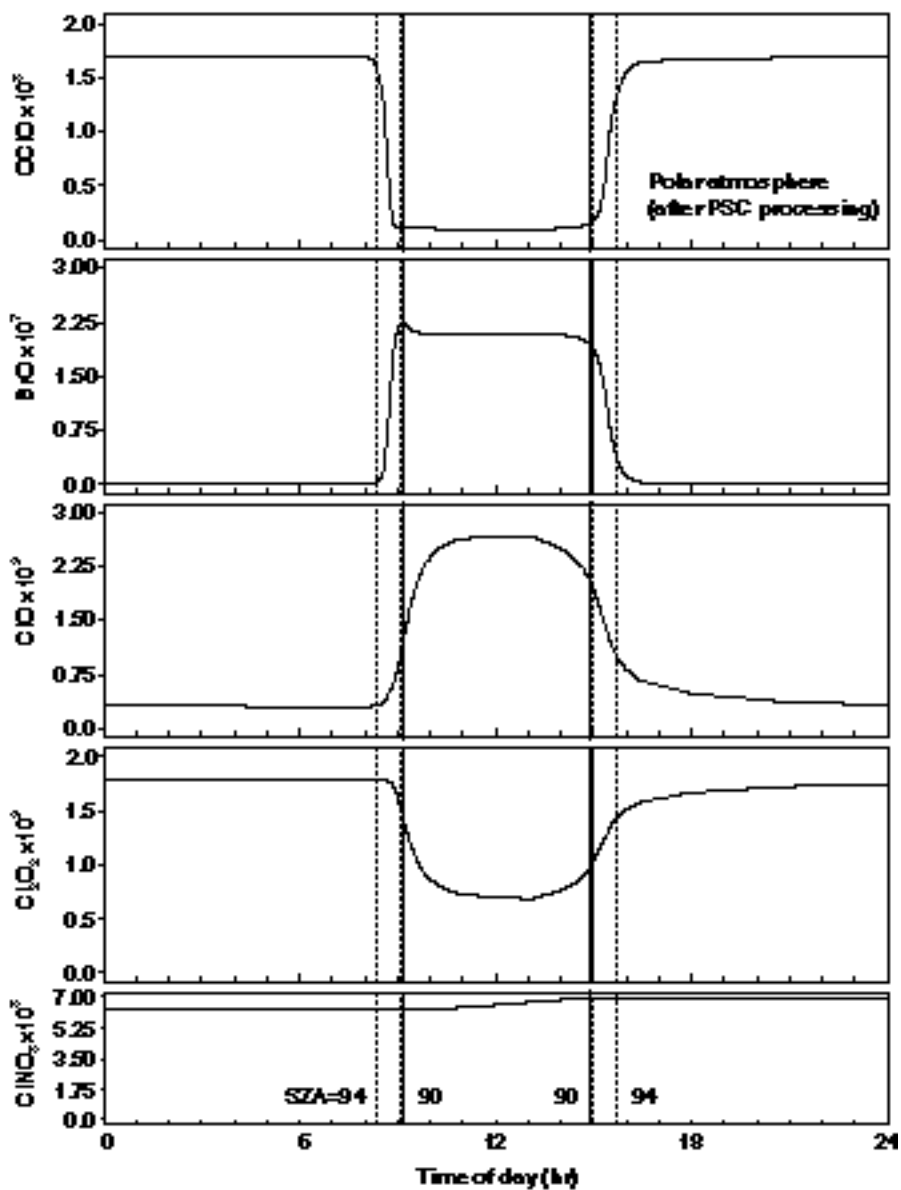


Figure 2.2.1 (a)

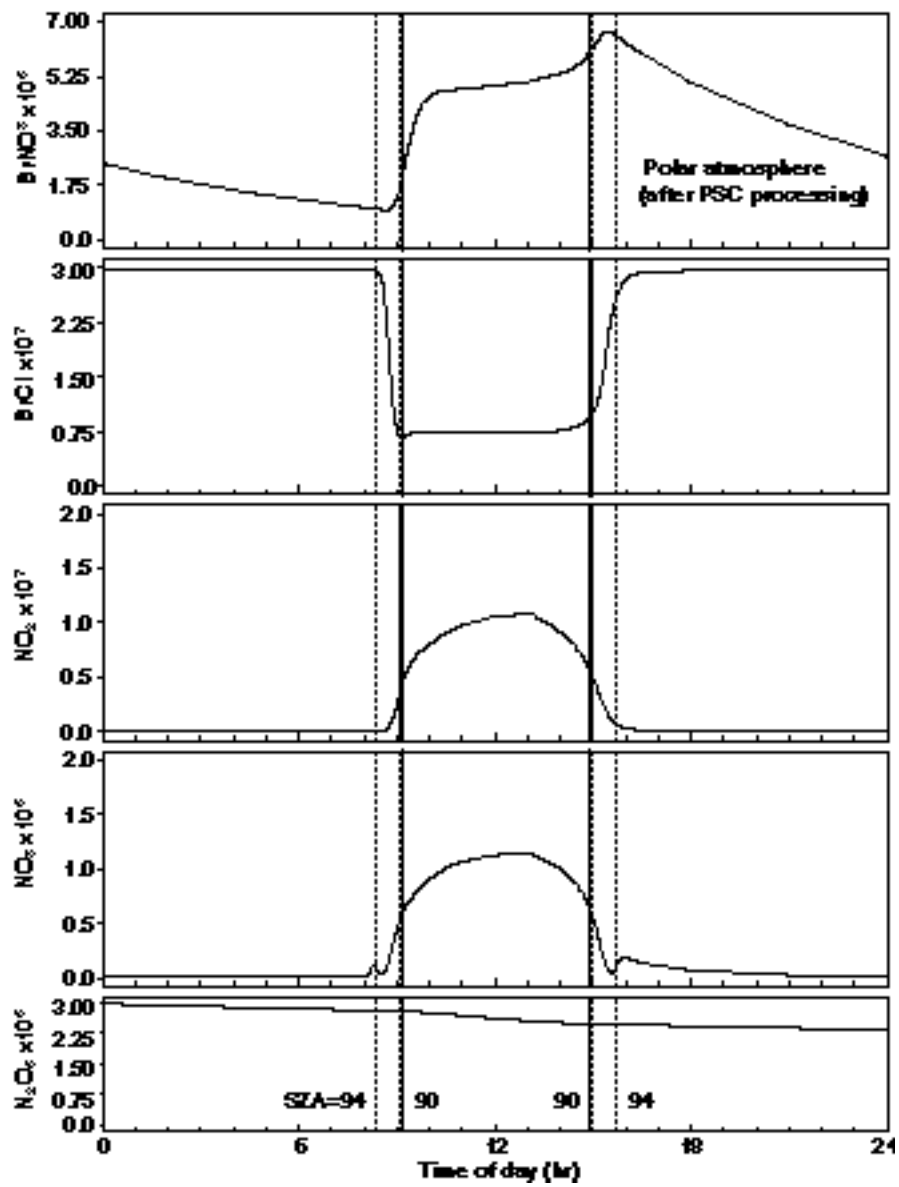


Figure2.2.1(b)

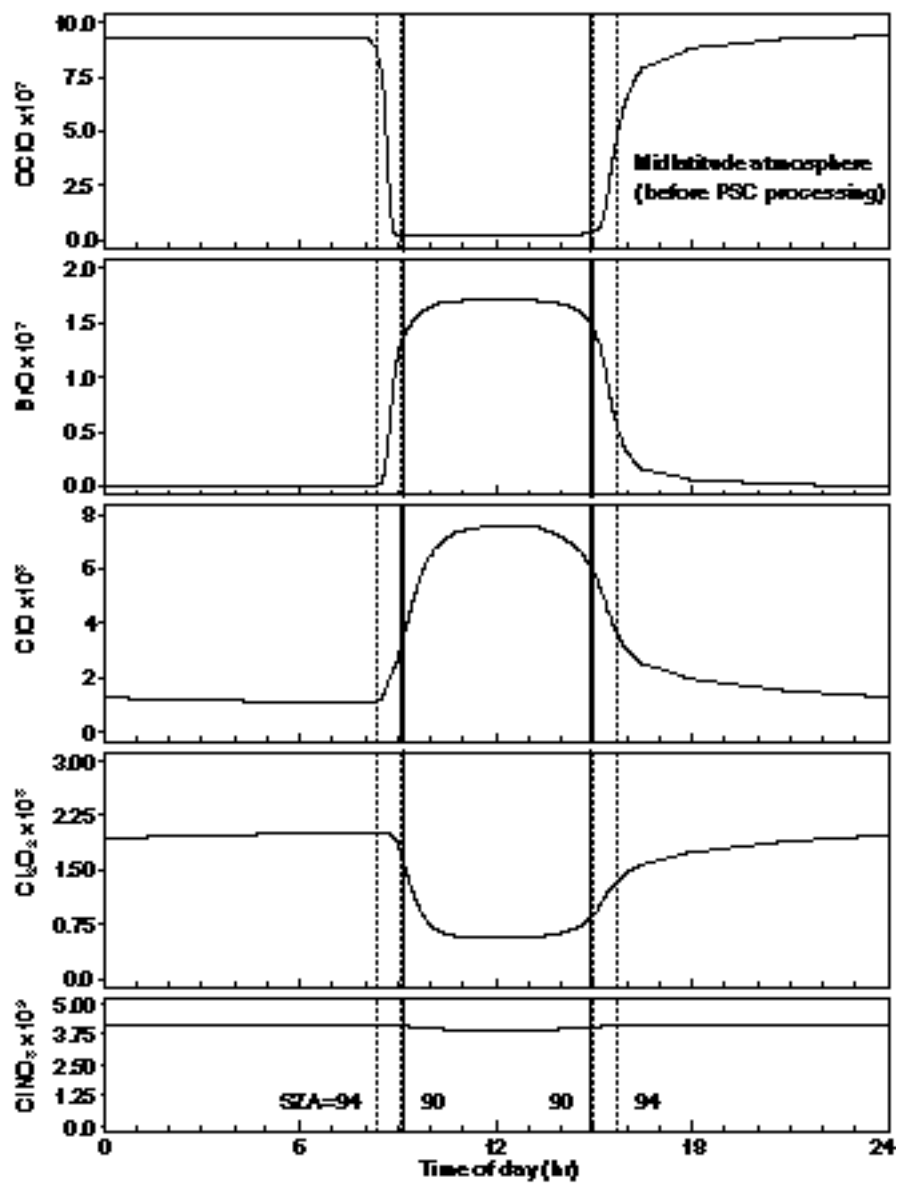


Figure 2.2.1(C)

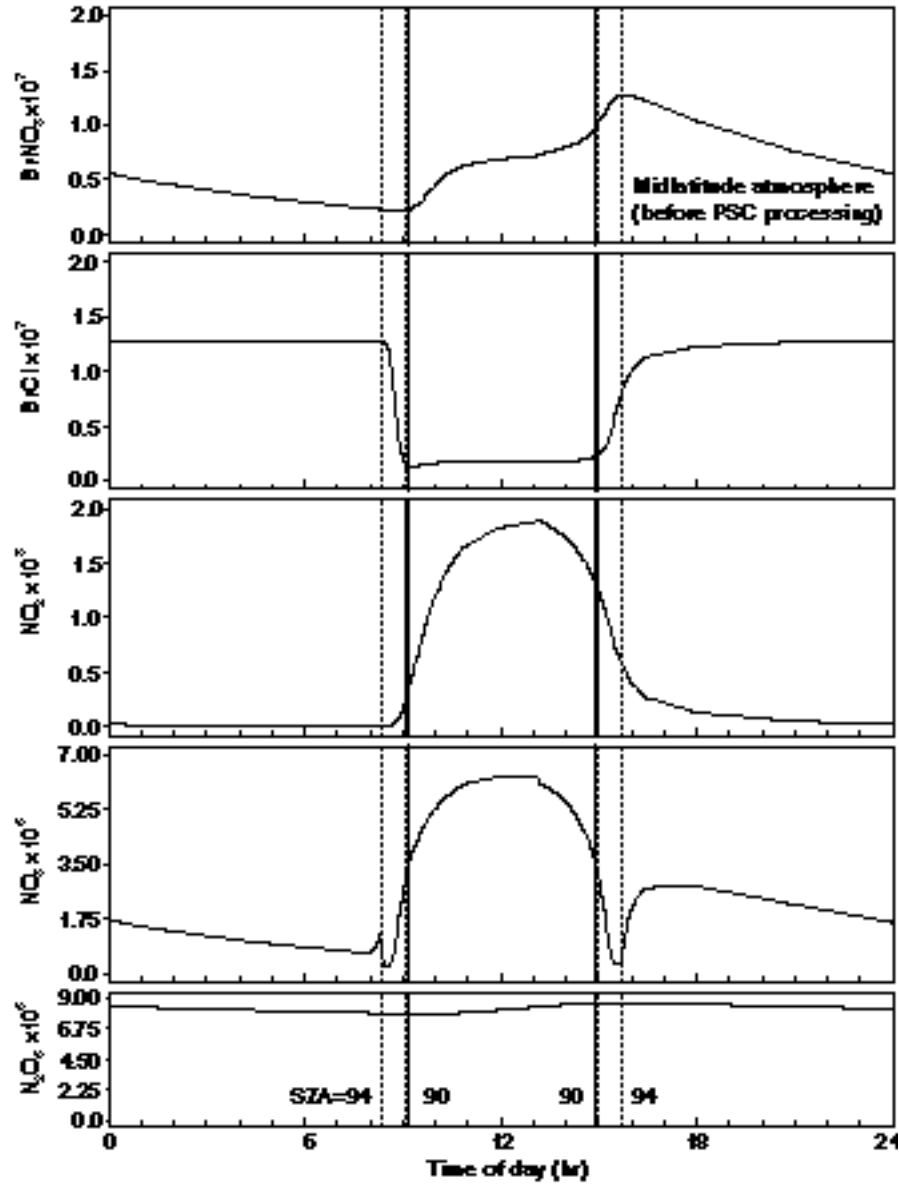


Figure 2.2.1 (d)

Figure 2.2.1 Diurnal variation of polar processed and pre-polar processed air obtained with conditions: Altitude = 20 km, latitude = -66, solar declination = +22.4, temperature = 198 K, $Cl_y = 3 \times 10^9 \text{ cm}^{-3}$, $Br_y = 2.65 \times 10^7 \text{ cm}^{-3}$.

(a, b). Diurnal curves (concentration vs time) are presented for a case where 15% of HCl has been converted to ClO_x ($= ClO + 2x(ClO)_2 + ClNO_3$) and 90% of steady-state $NO_x + ClNO_3$ has been converted to HNO_3 .

(c, d). Diurnal curves are presented for air prior to polar processing, all other conditions the same: $NO_x + ClNO_3 = 0.11 \times NO_y$.

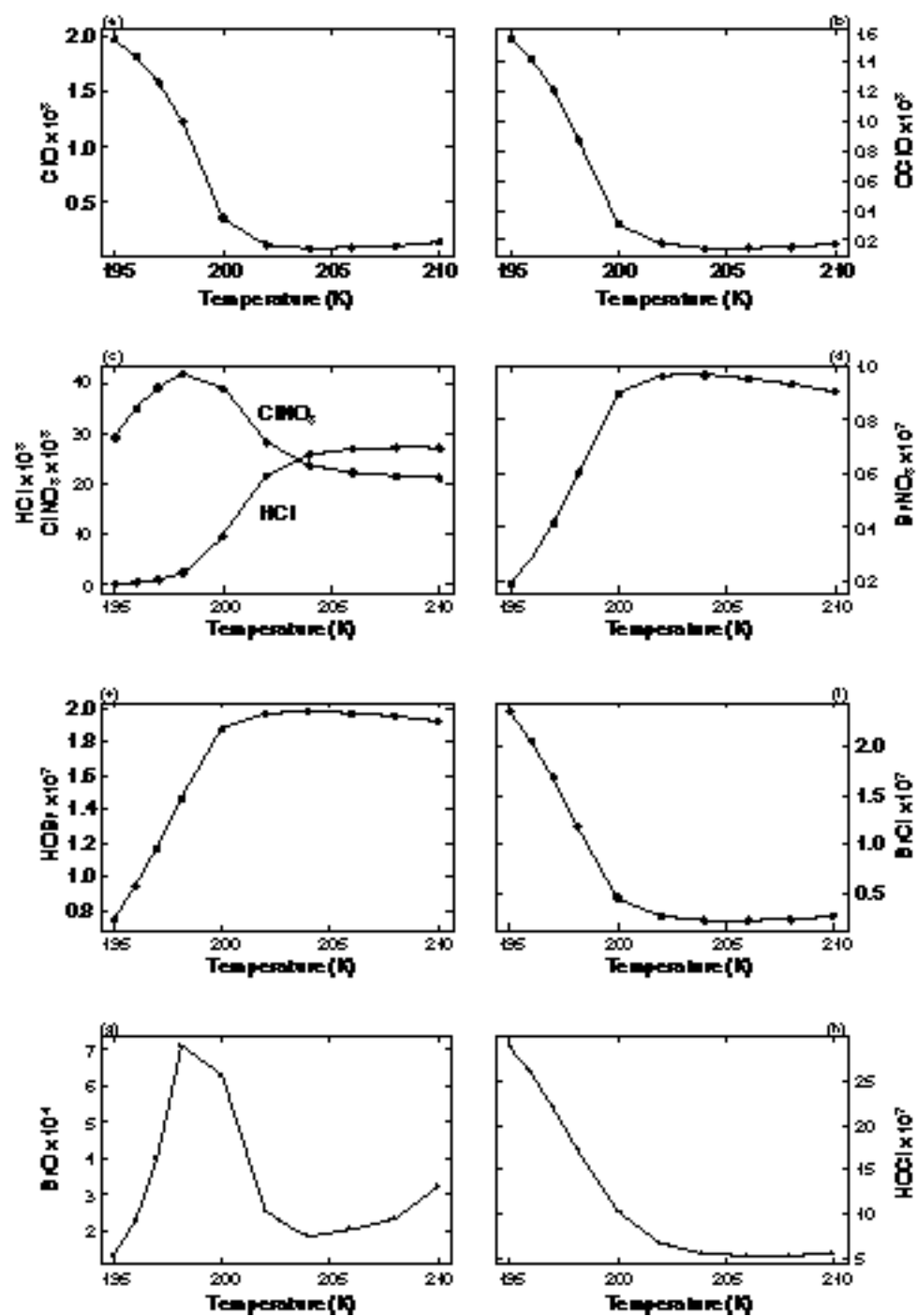


Figure 2.2.2(a-h)

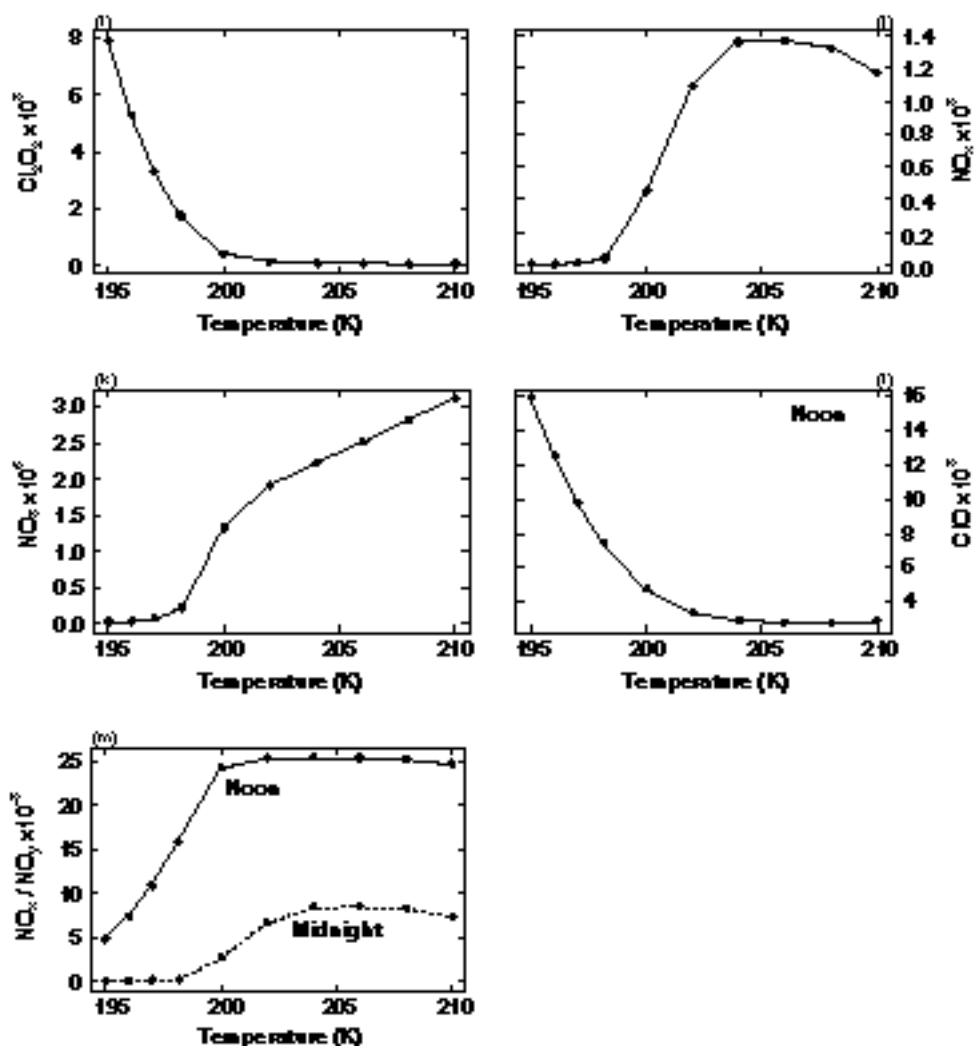


Figure 2.2.2(i-m)

Figure 2.2.2 Concentrations of radicals and reactive reservoir species as a function of temperature, for the conditions in Figure 2.2.1(c,d). Values represent midnight conditions for a computation where the system has relaxed to a diurnal steady-state (values repeat each day with no long-term trend). (a) ClO, (b) OCIO, (c) ClONO₂ and HCl, (d) BrNO₃, (e) HOBr, (f) BrCl, (g) BrO, (h) HOCl, (i) Cl₂O₂ (ClO dimer), (j) NO_x, (k) NO₃, (l) ClO at noon, (m) NO_x/NO_y at noon and midnight.

3.0 Algorithm Description

3.1 Introduction

3.1.1 Physical Description

SAGE III is designed to measure the attenuation of solar radiation by the Earth's atmosphere due to scattering and absorption by atmospheric constituents during each sunrise and sunset encountered by its spaceborne platform. In addition, SAGE III will make measurements during moonrise and moonset when the atmosphere is not directly illuminated by the Sun. SAGE III consists of three subsystems: the pointing, the imaging, and the spectrometer subsystems. The pointing subsystem consists of a scan mirror which acquires the radiant target (either the Sun or the Moon), and performs vertical scanning (with respect to the Earth's horizon) across the target. A measurement is considered to occur at the point along the line of sight (LOS) from the instrument to the target at which it comes closest to the Earth's surface (i.e., the sub-tangent point). The altitude of that point above the Earth's surface is commonly referred to as the tangent altitude. The imaging subsystem produces a focused image of the target at a focal plane where the "science" aperture, that defines the instrument's instantaneous field of view (IFOV), is situated. The SAGE III IFOV is 30 arcseconds in the vertical direction which translates to approximately 0.5 km at the tangent altitude. The spectrometer subsystem is situated behind the science aperture and consists of an 800-element CCD to measure solar radiation from 280 to 1040 nm with 1 to 2 nm spectral resolution. An additional photodetector is used to measure radiation at 1550 nm.

The viewing geometry of a solar occultation event is illustrated in Figure 3.1.1.1. During an event, the spacecraft motion relative to the Sun's (or Moon's) location permit the measurement of atmospheric transmission at tangent altitudes from the Earth's surface to well above the atmosphere. Since the instrument continually scans vertically across the target, and both the Sun and Moon subtend 32 arcminutes, the transmission at each tangent altitude is measured many times during an event. In addition, by measuring the unattenuated target (along LOS's which do not intersect the Earth's atmosphere) the instrument is recalibrated during each event. Therefore, the instrument provides not only accurate, high vertical resolution measurements of atmospheric transmission, but measurements which are relatively immune to drift in instrument performance.

Figure 3.1.1.2 illustrates the operation of the SAGE III instrument during a typical sunrise event. The two solid lines in the figure represent the upper and lower edges of the Sun as viewed from the spacecraft during the course of the event. The apparent narrowing of the solar image in the lower atmosphere is the result of refraction. The "saw-tooth" line represents the relative motion of the instrument mirror as it scans across the Sun at a nominal rate of 15 arcminutes s^{-1} . As soon as the instrument acquires the Sun in the lower atmosphere, the initiation of a sunrise event, the IFOV is centered long the radiometric

center of the solar image and the scan mirror will move up and down to provide vertical scanning of a solar disk. The scanning motion continues until the tangent altitude reaches 300 km. Figure 3.1.1.3 shows an example of the measured radiance (expressed in counts) for a SAM II 1000 nm event. The scans are alternately upscans and downscans following solar acquisition. Note the peak intensity of each scan gradually increases until it is constant after approximately 40 s, indicating that the Sun is above the atmosphere. In this example, the attenuation in the lower atmosphere is dominated by Rayleigh and aerosol scattering.

The occultation technique is rather unique in that the measurement coverage, both spatial and temporal, is strongly linked to the orbit parameters of the spacecraft. With one of the prime scientific objectives being the determination and monitoring of trends in atmospheric constituents, SAGE III must be deployed in a fashion which yields adequate spatial (latitudinal) and temporal (seasonal) coverage. The current planned implementation for SAGE III is to place one instrument in a sun-synchronous orbit and another, concurrently, in a mid-inclination orbit. The addition of a second occultation target, the Moon, increases the sampling and offers complementary coverage, for example, the ability to make measurements during the polar winter night where sunrises and sunsets do not occur.

The spectral variation of atmospheric extinction is illustrated in Figure 3.1.1.4 showing the contribution of atmospheric extinction versus wavelength from the different constituents at an altitude of 18 km. Both aerosol and Rayleigh scattering contribute at all wavelengths. Ozone has strong absorption in the Hartley-Huggins band (UV) and the Chappuis band in the visible. NO_2 absorbs between 350 and 600 nm. Water vapor has absorption lines throughout the visible, but with a strong band near 940 nm. NO_3 has absorption features between 500 and 650 nm, and OCIO has a strong band at 350 nm. SAGE III utilizes the spectrometer with the CCD detector to provide spectral measurements over the wavelength ranges from 280 to 1040 nm so that all of these gaseous species can be detected. An additional channel at 1550 nm is used for near IR aerosol extinction measurements. While SAGE III makes 800 individual spectral measurements, in practice only 70-80 discrete values (combinations of 1 or more digitized CCD element measurements) will be routinely transmitted to the ground. These are sufficient to retrieve all gaseous species and aerosol parameters.

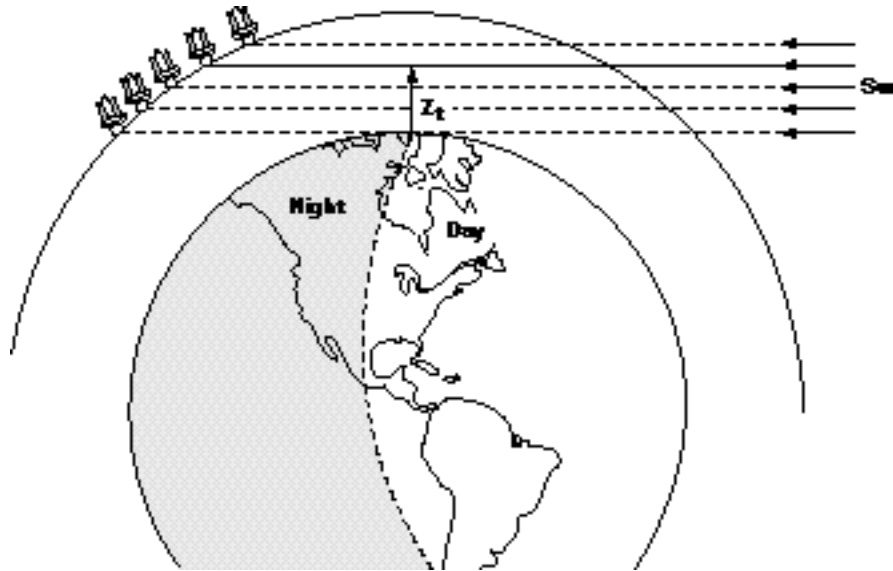


Figure 3.1.1.1 SAGE III Solar occultation measurement geometry. The tangent altitude is denoted by Z_t .

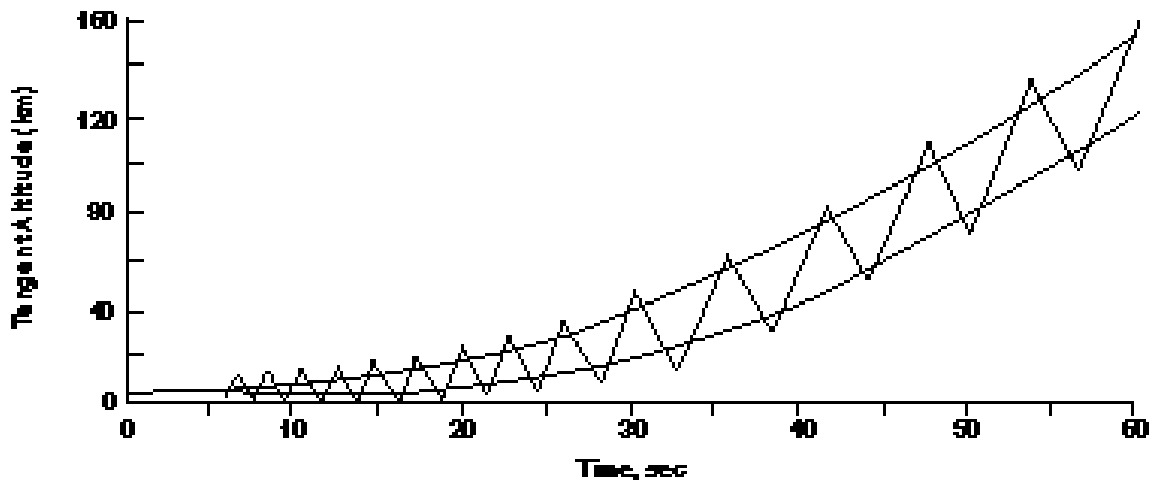


Figure 3.1.1.2 Typical sunrise event: lines indicate position of top and bottom of the Sun, and scan motion of SAGE scan mirror across the solar disk.

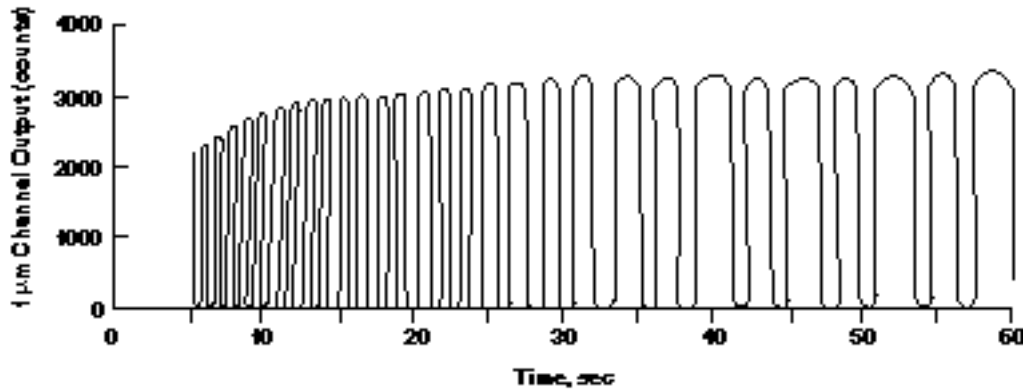


Figure 3.1.1.3 An example of 1 micron extinction from SAM II during a sunrise event.

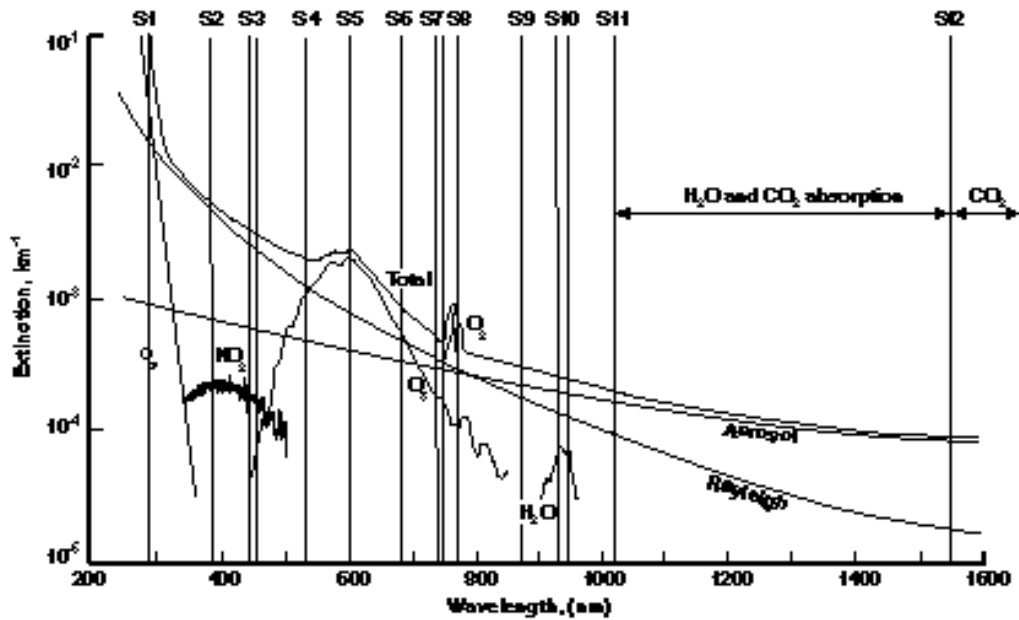


Figure 3.1.1.4 Wavelength dependence of atmospheric extinction at 18 km (NO_3 and ClO are not shown).

3.1.2 The Forward Problem

The equation of radiative transfer in one dimension for radiance, $I(\lambda, x)$, at wavelength λ , at an arbitrary point x is given by

$$\frac{dI(\lambda, x)}{d(\lambda, x)} = S(\lambda, x) - I(\lambda, x), \quad (3.1.2.1)$$

where S is the source function and $d(\lambda, x)$ is the optical depth between points x and $x+dx$. The optical depth per unit distance ($d(\lambda, x)/dx$) is commonly referred to as extinction. The source function consists of contributions from both single and multiple scattering as well as emission. For SAGE III measurements, wavelengths, and geometry

(directly observing the Sun through a small IFOV), scattering and emission terms are very small relative to the directly transmitted component and can be ignored. Therefore, Equation 3.1.2.1 can be simplified to

$$\frac{dI(\lambda, x)}{dx} = -I(\lambda, x). \quad (3.1.2.2)$$

The solution to this equation, when the unattenuated radiance (at $x=0$) is given by $I(\lambda, 0)$, is given by

$$I(\lambda, x) = I(\lambda, 0)e^{-\tau(\lambda, x)}. \quad (3.1.2.3)$$

Then, the irradiance, R_N as measured by SAGE III for channel “N”, can be expressed as

$$R_N(Z_t) = \int_0^\infty \int_{-\theta/2}^{\theta/2} I(\lambda, 0)e^{-\tau(\lambda, Z_t)} W(\lambda) d\lambda d\theta, \quad (3.1.2.4)$$

where $\tau(\lambda, Z_t)$ is the optical depth along the line of sight at tangent height Z_t between the instrument and the Sun, $\Delta\lambda$ is the spectral width of channel N with band pass function $W(\lambda)$, θ is the angular field of view of the instrument with response $W(\theta)$. The value of $\tau(\lambda, Z_t)$ varies with tangent altitude; it is effectively 0 above 100km and generally increases downward. It is composed of contributions from Rayleigh, aerosol, and gaseous species extinction. Transmission along the line of sight, $T_N(Z_t)$ (also called the slant path transmission), at tangent height Z_t , is defined as

$$T_N(Z_t) = R_N(Z_t) / R_N(Z_t^*), \quad (3.1.2.5)$$

where (Z_t^*) is a tangent altitude well above the atmosphere (> 100 km).

3.2 Retrieval Algorithm Description

3.2.1 Overview and Assumptions

In as much as SAGE III is a fourth generation instrument, the operational software also represents a fourth level in the complexity of the species separation algorithm. The earliest instrument, the Stratospheric Aerosol Measurement (SAM II) (1978-1994) was a single channel (or wavelength) instrument where external Rayleigh or molecular scattering effects were subtracted from the line of sight optical depths. Subsequently, the remaining optical depth peeled to a vertical profile of aerosol extinction at 1000 nm. The first Stratospheric Aerosol and Gas Experiment (SAGE) (1979-1981), and its follow-on mission SAGE II (1984-present), used measurements (often referred to as “channels”) of atmospheric line-of-sight transmission at multiple wavelengths (four and seven, respectively) from the ultraviolet to the near-infrared. These extra channels were employed to infer vertical profiles of multi-wavelength aerosol extinction, ozone (O_3), nitrogen dioxide (NO_2), and,

in the case of SAGE II, water vapor (H_2O). These instruments also introduced a new challenge: separating the effects of different species when they affect transmission at more than one measurement wavelength [Chu et al., 1989]. While these experiments were highly successful, the extent of mutual interference limited the vertical domain and the accuracy of each species retrieved.

For solar occultation events, SAGE III uses 87 channels between 290 and 1540 nm at which vertical profiles of transmission are determined. This data is used to produce profiles of the molecular density of O_3 , NO_2 , H_2O , aerosol extinction at 9 wavelengths, cloud presence, temperature, and pressure. With this in the spectral density of the channels, the inversion algorithm has been designed to minimize past difficulties with species separation and improve both the accuracy and vertical range of the data products. In addition, it adds new aerosol extinction channels (up to 9 wavelengths), formalizes cloud presence as a data product, and temperature and pressure profiling through the use of the oxygen A Band located near 765 nm. The process or algorithm that leads from raw instrument counts to data products can be broken into two distinct parts: the transmission algorithm and the species inversion algorithm. The different steps in the transmission and inversion algorithms and the overall flow of the algorithm are illustrated in Figure 3.2.1.1. Details of the transmission algorithm may be found in the SAGE III Transmission ATBD (LaRC475-00-108). A brief overview of the transmission algorithm follows. The species-inversion algorithm overview is discussed in Section 3.2.2. The species-specific segments of the algorithm are found in 3.2.3.

Transmission Algorithm Summary

The function of the transmission algorithm is to produce multi-wavelength slant path transmission profiles from time sequences of radiometric and engineering measurements by the SAGE III instrument. As shown in Figure 3.2.1.1, this process can be separated into five components: data screening, position registration, altitude registration, wavelength registration, and data grouping and statistics. The first step in the transmission algorithm is the screening of the input level zero (telemetry) data. The data-screening algorithm locates missing or bad data and determines whether the data are recoverable. Next, the position registration algorithm determines solar point positioning and the tangent height. The tangent height is the altitude at which the ray is closest to the Earth's surface for the line-of-sight that originates from the center of the instrument's field of view to the position on the sun. Taking the ratio of the science scan data (any data with an associated tangent height below 100 km) relative to the same solar position on exo-atmospheric scans produces atmospheric transmission for an individual measurement. The tangent height calculation provides the height registration of the derived transmission values. Generally, tangent height is dominated by geometric concerns, however it is corrected for atmospheric refraction, which becomes increasingly significant below 30 km. Each channel is also calibrated for wavelength using an operation mode of the instrument that occurs at tangent altitudes well above normal operation regions in the atmosphere. Using all 800 pixels, a multi-linear

regression procedure is used to assign spectral positions to individual pixels by using a standard solar spectrum. The solar spectrum has complex spectral features including the solar Fraunhofer lines that measured by the SAGE III CCD spectrometer system. In this manner, shifting and stretching of the pixels on the CCD device due to thermal or mechanical perturbations can be accounted for and the center wavelength for each of the 800 pixels will be accurately determined. The final step in the transmission algorithm is the data grouping and statistics. This procedure takes the individual transmission data (up to several thousand data points per channel) into altitude profiles and performs statistical analyses to determine the characteristics of the distribution of the measured data in each group. Transmission profiles for each channel are produced on a 0.5-km grid from 0.5 km to 100 km with an uncertainty estimate. The correlation between channels at 521, 1020 and 1540 nm at altitudes between 6.5 and 26.5 km is also calculated as required input to the cloud presence algorithm.

3.2.2 Species Separation Algorithm

The species separation algorithm involves the inversion of the multi-wavelength slant path transmission profiles into vertical profiles of the molecular density of SAGE III-measured gas species as well as aerosol extinction at several wavelengths between 290 nm and 1550 nm. For most species, rather than work directly from transmission profiles $T(z_t)$, the inversion algorithm works with the slant path optical depth, $\tau(z_t)$, which can be expressed for wavelength, λ , and slant path tangent height, z_t , as

$$\tau(z_t) = -\ln(T(z_t)). \quad (3.2.2.1)$$

The slant path optical depth at each SAGE III measurement wavelength consists of several components including molecular or Rayleigh scattering, aerosol extinction, and usually absorption by one or more gaseous species. At each tangent height, SAGE III will make measurements at 87 wavelengths (or channels) between 290 nm and 1540 nm distributed as shown in Table 3.2.2.1. The ensemble of SAGE III measurements at a given tangent height can be expressed a series of linear equations of the form

$$\tau = \tau_R + \tau_a + \sum_{n=1}^N \tau_{gn}, \quad (3.2.2.2)$$

where τ_R is the Rayleigh slant path optical depth, τ_a is the aerosol slant path optical depth, and τ_{gn} is the slant path optical depth for gas species n, where N can be from 0 to 4. A crucial element of the inversion process is the partitioning of the total slant path optical depth at each wavelength and tangent altitude into the contributions of the individual components. Thus, for the measurement ensemble, there are unknown molecular and aerosol components at each wavelength, unknown temperature and pressure, as well as unknown ozone, nitrogen dioxide, and water vapor molecular densities, or, in a nominal sense, more than twice as many unknown parameters as measurements at each tangent altitude. Table 3.2.2.1 lists the primary and interfering species for each channel.

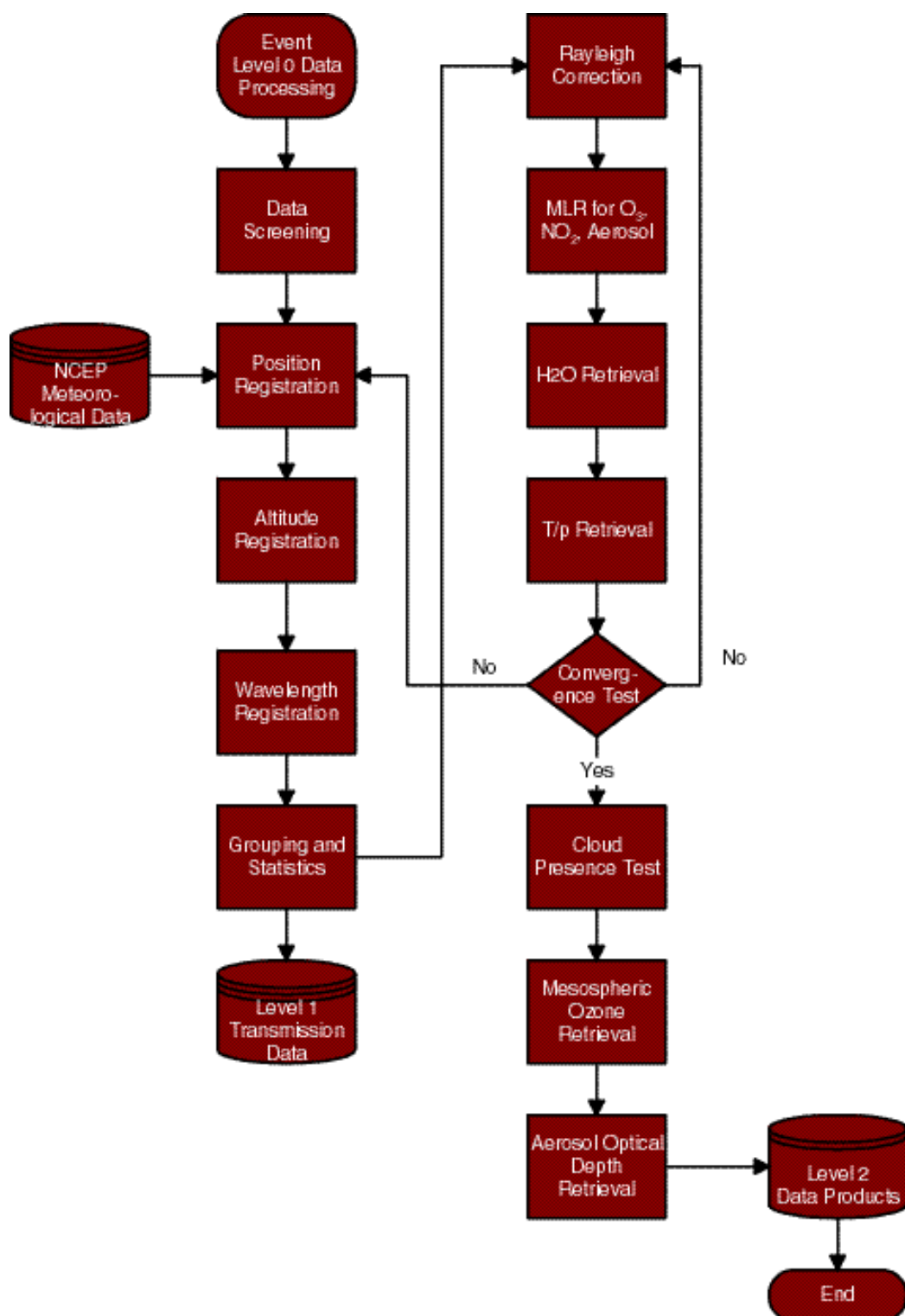


Figure 3.2.1.1 Flow of data through the SAGE III processing algorithm.

Table 3.2.2.1 SAGE III Channel Groupings with Primary and Interfering Species.

Channel Grouping		Primary Species	Interfering Species+
S1	290 nm	O ₃	
S2	385 nm	Aerosol	NO ₂ , O ₃
S3	433-450 nm	NO ₂ , Aerosol	O ₃
S4	521 nm	Aerosol, Cloud	NO ₂ , O ₃
S5	563-622 nm	O ₃ , Aerosol	NO ₂ , H ₂ O
S6	676 nm	Aerosol	O ₃
S7	758 nm	Aerosol	O ₃
S8	759-771 nm	O ₂ (T,P)	O ₃
S9	869 nm	Aerosol	O ₃ , H ₂ O
S10	933-960 nm	H ₂ O	O ₃
S11	1020 nm	Aerosol, Cloud	O ₃
S12	1540 nm	Aerosol, Cloud	CO ₂ , H ₂ O

+ Any species influencing the retrieval of the primary species except the omnipresent Rayleigh and aerosol components.

The Rayleigh contribution has a well-known wavelength dependence (λ^{-4}) and is dependent only on the total molecular mass along the slant path. Formally, this can be expressed as

$$R = \int_{z_f}^z \rho(z) dx(z, z_f), \quad (3.2.2.3)$$

where R is the Rayleigh mass extinction coefficient determined using the formulation of Bucholz (1996). And $\rho(z)$ is the molecular mass density as a function of height and determined from the current values for the temperature and pressure profiles and the ideal gas law, and $dx(z, z_f)$ is the length of the slant path between the altitudes of z and $z+dz$ and includes the effects of spherical geometry and wavelength-dependent refraction [Chu, 1983]. Like the refraction component of the transmission algorithm, the unknown Rayleigh slant path optical depth is initially estimated using temperature and pressure profiles supplied by the NCEP and the GRAM 95 climatology (for altitudes above 50 km). A branch back to either refraction module or the Rayleigh calculation may be required if the temperature and pressure product is the difference between the final product and the initial guess is sufficiently large.

The next step in the inversion process is to derive slant path number density profiles for NO_2 and O_3 using multiple linear regression (MLR) and the channels for these species listed in Table 3.2.2.1 (S3 and S5). The advantage of this procedure is that the fine structure of these species, particularly NO_2 , in these bands permits the extraction of the column densities independently of either the aerosol or molecular components. It is necessary to simultaneously solve for these species since they absorb significantly in both spectral regions (433-450 nm and 562-622 nm). The MLR inversion process is discussed in detail in Section 3.2.3 of the NO_2 , NO_3 , OCIO , and O_3 ATBDs (LaRC475-00-101, LaRC475-00-102, LaRC475-00-103, LaRC475-00-107, respectively). Once the slant-path column densities have been derived, the influence of NO_2 and O_3 is removed from all measurement wavelengths in which it is a component excluding the mesospheric ozone channel at 290 nm. The slant path aerosol optical depths for the nominal SAGE III aerosol channels at 385, 448, 521, 595, 676, 758, 869, 1020, and 1540 nm (involving S2-S7, S9, S11 and S12). They are retrieved as residuals of the MLR retrievals of O_3 and NO_2 and thus are effectively a part of the MLR procedure.

In both the center of the ozone Chappuis band and in some of the aerosol channels, water vapor is a minor contributor that cannot be initially corrected. Thus, in the first iteration, the water vapor correction in these channels will be neglected. While, for subsequent iterations, it will be determined using the current retrieved water vapor profile using the method described in Section 3.2.3 of the SAGE III Water Vapor ATBD (LaRC475-00-100).

The next stage in the retrieval process is the retrieval of the water vapor profile. Since both aerosol and ozone significantly contribute in the SAGE III water vapor channels between 933 and 960 nm (Table 3.2.2.1), the first step in the water vapor retrieval algorithm is to isolate the water vapor contribution. The effects of ozone can be estimated using the MLR ozone product and the appropriate cross sections. For aerosols, we have initially implemented a simple multi-channel interpolation to remove the influence of aerosol using the aerosol derived as a part of the MLR procedure. This is similar to the approach used with earlier SAGE inversions however, the increase in number and proximity of aerosol channels greatly improve this approach and modeling indicates that this is sufficient for most circumstances. However, more robust approaches are under investigation that allow the retrieval to estimate both the water vapor profile, aerosol, and ozone effects independently of estimates of aerosol and ozone based on measurements at other wavelengths. This may be particularly advantageous for ozone effects since the temperature dependence of ozone absorption in the water vapor feature is not well known and the magnitude of ozone absorption may exceed that of water vapor at some altitudes. With the current method, given the profile of water vapor slant path optical depths, the vertical profile of water vapor density is solved for using the procedure described in Section 3.2.3 of the SAGE III Water Vapor ATBD (LaRC475-00-100). It is a standard Levenberg-Marquardt inversion that, unlike aerosol, O_3 , and NO_2 (which remain in slant path format at this point of the inversion process), directly produces a vertical profile of water vapor

molecular density. The derived water vapor profile may be used on subsequent iterations to remove the influence of water outside the nominal water vapor band. In particular, water vapor absorbs weakly near 600 nm (and thus influences ozone retrievals) as well as at 869 nm (influencing the aerosol extinction measurement at that wavelength).

The next stage in the retrieval process is the retrieval of temperature and pressure (T/p). Like water vapor, aerosol and ozone contribute in a generally small but significant way to the total optical depth in the SAGE III O₂ A-Band channels between 759 and 771 nm (Table 3.2.2.1). As for the water vapor retrieval, we have initially implemented a simple multi-channel interpolation to remove the influence of aerosol using the aerosol slant path optical depth derived as a part of the MLR procedure. In addition, again, the effects of ozone can be estimated using the MLR ozone product and the appropriate cross sections. Once those species have been accounted for, the residual values are the slant path oxygen A-band optical depths. Given the profile of oxygen A-band slant path optical depths (at 14 channels), the vertical profiles of temperature and pressure are determined using a non-linear Marquardt-Levenberg method described in Section 3.2.3 of the SAGE III Temperature & Pressure ATBD (LaRC475-00-104). Like the water vapor inversion algorithm, the T/p procedure yields vertical profiles rather than slant path profiles.

Both the water vapor and the temperature and pressure retrieval algorithms require a forward model as part of the retrieval process. We have implemented the Emissivity Curve-of-Growth Approximation (EGA). Testing suggests that it is adequate and far quicker than line-by-line calculations.

At this point of the retrieval process, it is possible that branching backward in the retrieval process is possible. While unlikely, it is possible that the change in atmospheric density (as inferred by the T/p retrieval) to be sufficiently large to change altitude registration performed in the transmission section of the retrieval process. In this case, the processing branches back to the refraction computation segment of the transmission calculation. It is also possible that the processing could branch back to the Rayleigh optical depth or water vapor sections of the species separation algorithm if the change in the estimated Rayleigh correction profile exceeds the estimated uncertainty in those profiles. Otherwise, the processing branches to the final stages of the inversion process. The branching process will be run-time controllable feature.

The final stages of the retrieval algorithm are mesospheric ozone retrieval, profile peeling, cloud presence detection, and aerosol stratospheric optical depth calculation. The mesospheric ozone algorithm makes use of the 290 and 385 nm line-of-sight optical depths (uncorrected for Rayleigh). This is a straightforward algorithm and discussed in the SAGE III Ozone ATBD (LaRC475-00-107). Profile peeling (the conversion from line-of-sight or slant path optical depth to extinction profile or number density) follows the SAGE II processing method in which a modified-Chahine method [Chahine; 1972, Twomey, 1975.

Chu and McCormick, 1979; Chu, 1985; Chu *et al.*, 1989] was employed, though alternative methods are available as runtime options including simple onion peeling.

The Cloud Presence Algorithm is detailed in SAGE III Cloud ATDB (LaRC475-00-106) and makes use of aerosol extinction at 521, 1020, and 1540 nm between 6.5 and 26.5 km. The basic algorithm relies upon wavelength ratios between these aerosol extinction in these channels (clouds tend to be “white”) but also requires a separate user driven quality control process for which a separate document is being developed.

With all species transformed to vertical profiles, construction of the data products listed in Table 1.2.1 is executed and the data made available for archival.

Uncertainty Estimation

Satellite measurements contain uncertainty that includes both random and systematic components. As in the SAGE and SAGE II retrievals, the SAGE III measurements will provide uncertainty estimates for random components [Russell *et. al.*, 1981; Chu *et. al.*, 1993]. In the case of systematic uncertainty, it is normally secondary and can be assessed through sensitivity analysis. There are three primary sources of the random component of the uncertainty (a) line-of-sight optical depth measurement errors, (b) the Rayleigh optical depth estimate, and (c) uncertainties resulting from the removal of contributions by interfering species. The basic concept of the reported SAGE III data-products uncertainties is the transference of measurement error to data product error via the mathematical processes that produce them.

The grouping and statistics algorithm described in the SAGE III Transmission ATDB determines errors in the line-of-sight optical depth (or its companion transmission). The measurement error can be modified by the removal or clearing of the species which are considered to “interfere” with the retrieval process. This usually includes the Rayleigh component and, in some cases, one or more data products such as the removal of ozone from the water vapor and temperature/pressure channels. If branching back occurs, the Rayleigh uncertainty would be modified and water vapor uncertainty included at the appropriate channels. This modified error then becomes the base measurement error.

The method by which these uncertainties propagate into species is greatly dependent on method employed. For instance, MLR error in the line-of-sight values is a product of the MLR mathematical process measurement spectrum and not strongly dependent on the estimated signal error. This is described in more detail in the O₃, NO₂, NO₃, and OCIO ATBDs and in common reference material [e.g., Bevington, 1969]. Since aerosol is predominately a residual of the MLR process its error is dominated by the measurement error and the species errors estimated by this algorithm.

To propagate errors determined for line-of-sight quantities (O_3 , NO_2 , NO_3 , $OCIO$, and aerosol) to the uncertainties in the vertical profile is a straightforward application of the least-squares form of onion peeling. The vertical profile of measurement variance (a vector, q) (uncertainty squared) is multiplied by the inverse of the path length matrix, P to produce the data product variance which can be expressed as

$$\underline{g} = P^{-1} \underline{q}$$

An element of the limb path length matrix contains the physical distance traversed by the line-of-sight ray path for a tangent layer n through layer m (non-zero only for $m \geq n$).

In the Marquardt-Levenberg method, (used by water vapor and T/p retrieval algorithms), covariance matrices are produced that translate measurement error into species uncertainties. In this case, since the products of these algorithms are the final data products no further modification of the estimated error is required.

Table 3.2.2.2 Uncertainty Estimates

Species	Expected Precision	Altitude Range
Aerosol 1020 nm, 521 nm	5%	0-40
Temperature	2 K	0-85
Pressure	2%	0-85
Ozone (Solar)	10%	6-85
Ozone (Lunar)	<10%	16-35
Nitrogen Dioxide (Solar)	15%	10-50
Nitrogen Dioxide (Lunar)	<10% <15%	22-32 19-37
Water Vapor	<5% 5%-15%	<33 33-42
Chlorine Dioxide	25%	15-25
Nitrogen Trioxide	10%	10-50

Note that systematic sources of error are neglected in discussion above. These arise primarily due to the degree to which basic physical assumptions are obeyed (e.g., spherical homogeneity; see Appendix C), imperfect knowledge of instrument performance, spacecraft ephemeris, and spectroscopy. An assessment of the current state of spectroscopy as it relates to SAGE III is given in Appendix D.

3.2.3 Differential Retrievals of Gases (Solar and Lunar)

Differential retrievals offer a direct computational means of separating aerosol extinction and gaseous absorption features. The following discussion focuses on the lunar occultation problem, but applies equally well to solar occultation, as will be the case for the retrievals of ozone and nitrogen dioxide.

Lunar occultation retrievals of atmospheric extinction are considerably more complicated than the solar occultation measurements as a result of the spatial and spectral non-uniformity of the surface albedo of the Moon. Consequently, the accuracy of the lunar limb-darkening curves that are used to calibrate each SAGE occultation event preclude the production of absolute transmission profiles during lunar occultation. Secondly, given the relatively low signal-to-noise ratios in lunar occultation measurements, single channel measurements are insufficient to meet the SAGE III measurement objectives; instead measurements from many channels are combined together to reduce the random measurement error (precision) to a level consistent with the performance goals for SAGE III lunar measurements. In the absence of an accurate exoatmospheric calibration, retrievals which utilize measurements over a broad spectral range must be performed in a fashion that is insensitive to broadband continua and extinction; one such approach is a differential measurement technique on the absorption spectrum. The observed lunar radiance is

$$I = aI_0 e^{-T} e^{-}, \quad (3.2.3.1)$$

where aI_0 is a scaled solar spectrum, and e^{-T} and e^{-} are broadband and narrowband (mostly atmospheric molecular absorption) features in the spectrum, respectively. The method under evaluation takes the natural logarithm of (3.2.3.1) to obtain

$$\ln(I / \bar{A} I_0) = \ln(Ae^{-T}) - . \quad (3.2.3.2)$$

The lunar albedo has been expressed as $\bar{A}A$, where \bar{A} is the mean albedo and A contains some spectral information unique to the Moon. In the case of solar occultation, $\bar{A}A$ is unity. Figure 3.2.3.1 depicts a scaled solar spectrum and figure 3.2.3.2 depicts a mean albedo. Strictly speaking the lunar albedo will probably have some higher frequency (narrow band) components which pass through the filter. For clarity, these terms will not be included in subsequent discussion and equations, however, they will be included in the retrieval. The observed lunar spectrum (I) has been divided by a scaled solar spectrum ($A I_0$). After taking the natural logarithm, terms may be separated in to broadband ($\ln(Ae^{-T})$) and narrowband, molecular () components. By definition, the term, , contains only the high frequency components of the observed spectra.

In order to obtain the term , the low frequency components

$$\ln(Ae^{-T}) \quad (3.2.3.3)$$

must be estimated. The filter types described below were developed and tested for evaluating (3.2.3.3) from the data. Each type was used to obtain the differential spectrum by subtracting the "low pass filter" result from the log of the ratio spectra.

1. A fast Fourier transform filter with an adjusted cutoff frequency to determine the low frequency components.
2. A finite impulse response filter to determine the low frequency components.
3. A least-squared fit to a second or third order polynomial to approximate the low-frequency components.
4. A singular value decomposition (SVD) fit to a second or third order polynomial to approximate the low frequency components.

The following techniques were tested in conjunction with each of the above filter types to improve the overall filter performance:

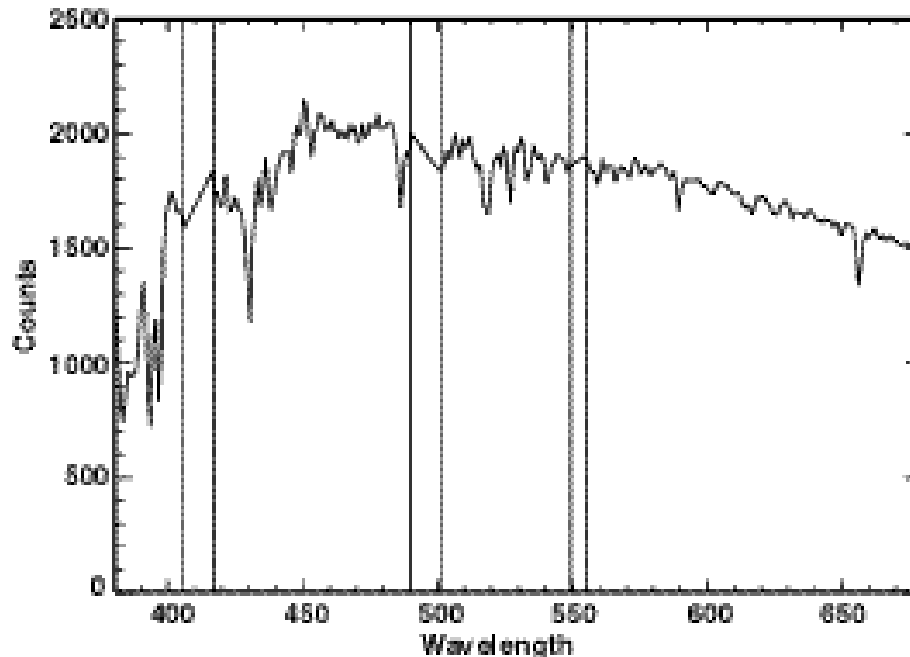


Figure 3.2.3.1 Scaled solar spectrum with channel gaps.

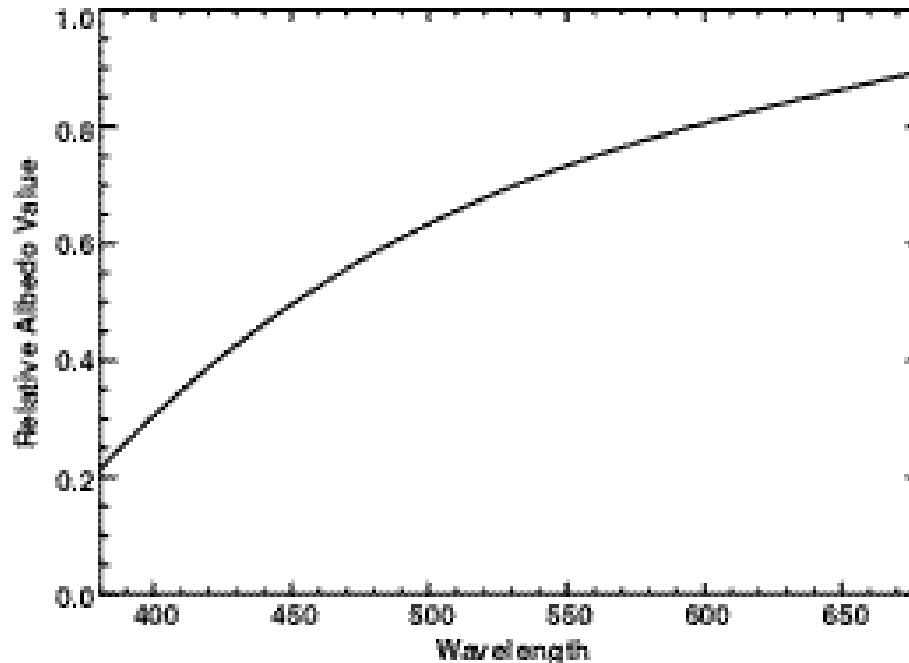


Figure 3.2.3.2 *Relative lunar albedo curve.*

1. The ratio data were filtered over wavelength intervals of various widths, with emphasis on the channel gaps depicted above, and using different combinations of polynomial order.
2. To smooth the data, the logarithm of the ratio data was taken, fitted with a low frequency wave form, and the exponential function of the fitted curve was subtracted from the original ratio data.
3. The ratio data were fitted with weighted curves to obtain an improved fit.

The best results for filtering the ratio data and removing the low frequency components were obtained by making a composite differential spectrum, by a combination of the above filter types and techniques, applied over different segments of the lunar pixel wavelengths. Figure 3.2.3.3 shows a composite differential spectrum at 25 Km. Additionally, using iterations and species clearing, (described in section below) in conjunction with filtering over a wider spectral range yielded a slight increase in the final retrieval accuracy. Ground-based measurements of the solar and lunar spectrum will be made using an engineering model of the SAGE III spectrometer (VU). These data will be used to refine the filtering scheme as well as to identify narrow band features in the lunar spectral albedo.

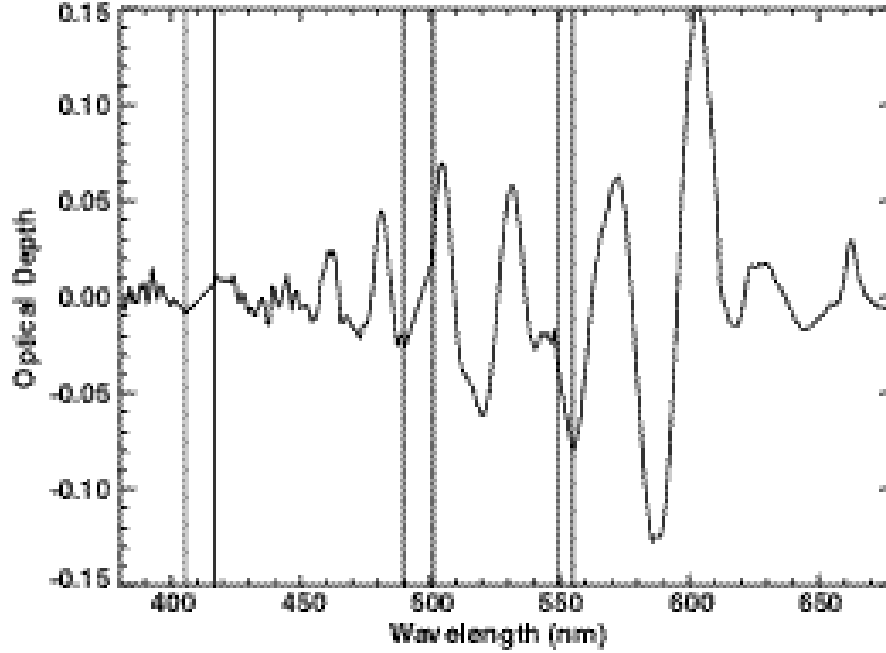


Figure 3.2.3.3 *Composite differential spectrum after filtering by segments.*

The differential spectrum is ideally suited for multiple linear regression analysis, as is indicated in the following sections. To optimize the number of channels available for analysis, the majority (~ 300) of the lunar occultation channels are contiguous between 380 and 680 nm, from which ozone, nitrogen dioxide, nitrogen trioxide, and chlorine dioxide will be measured. This differential spectrum will also contain any high frequency information contained in the lunar albedo and must be allowed for in the regression analysis. A channel selection for O₂ and H₂O will be similar to that used in solar occultation. Aerosol and cloud are not intended as standard products from the lunar occultation measurements.

Multiple Linear Regression

The formulation of the inverse problem after filtering the data follows the same methodology used in the aerosol/ozone retrieval problem

$$\begin{aligned} (i) = & n_{O_3} (i, O_3) + n_{NO_2} (i, NO_2) + n_{H_2O} (i, H_2O) + \\ & n_{NO_3} (i, NO_3) + n_{OCIO} (i, OCIO) \end{aligned} \quad (3.2.3.4)$$

or

$$(i) = \sum_k n_{ki} (i). \quad (3.2.3.5)$$

Alternatively, (i) maybe expressed in matrix form as

$$\begin{array}{cccccc}
380 & 380(O_3) & 380(NO_2) & 380(H_2O) & 380(NO_3) & 380(OCIO) & n_{O_3} \\
381 & 381(O_3) & 381(NO_2) & 381(H_2O) & 381(NO_3) & 381(OCIO) & n_{NO_2} \\
\cdot & \dots & \dots & \dots & \dots & \dots & n_{H_2O} \\
\cdot & \dots & \dots & \dots & \dots & \dots & n_{NO_3} \\
\cdot & \dots & \dots & \dots & \dots & \dots & n_{OICO} \\
680 & 680(O_3) & 680(NO_2) & 680(H_2O) & 680(NO_3) & 680(OCIO) &
\end{array} \quad (3.2.3.6)$$

or

$$T = SN, \quad (3.2.3.7)$$

where T is the measurement vector (N dimensional vector), N is the unknown species or solution vector (M dimensional), and S is the matrix relating the two vectors (N × M dimensional matrix) through their differential absorption spectra. The normal equations have the form

$$\sum_{i=1}^N \frac{1}{\sigma_i^2} \sum_{j=1}^M S_{ij} T_j = \sum_{i=1}^N \frac{1}{\sigma_i^2} \sum_{j=1}^M S_{ij}^2 N_j, \quad (3.2.3.8)$$

where the uncertainty σ_i has been included explicitly. In matrix form, this expression becomes

$$S^T T = [S^T S] N \quad (3.2.3.9)$$

with suitable representation of the weighted observations with T, the derived parameters by the vector N, and the normal matrix S. Since this is a well constrained set of equations, the solution to this set of linear equations can be found using a least-squares solution

$$N = [S^T S]^{-1} S^T T \quad (3.2.3.10)$$

or

$$n_j = \sum_{k=1}^M C_{jk} \sum_{i=1}^N \frac{1}{\sigma_i^2} S_{ik} T_i, \quad (3.2.3.11)$$

with the variance σ_j^2 of each derived parameters given by

$$\sigma_j^2(n_j) = \sum_{k=1}^M \sum_{l=1}^M C_{jk} C_{jl} \sum_{i=1}^N \frac{1}{\sigma_i^2} S_{ik} S_{il}, \quad (3.2.3.12)$$

where the covariance-correlation matrix $C = [S^T S]^{-1}$. The diagonal elements of C are the variances of the fitted parameters, and the off-diagonal elements are the covariance between species.

Simulated lunar occultation observations generated by a complex forward simulation model were used to begin development of differential MLR procedures. The simulation incorporated a solar spectrum ranging from 380 nm to 680 nm, reflected by a modeled lunar disk with variable albedo, ray tracing through the atmosphere, and the effects of Rayleigh scattering and absorption by molecular gases and aerosols. Chemical species absorption was simulated by using typical night time concentrations for O_3 , NO_2 , NO_3 , and OCIO. The key steps in the MLR retrieval process under development are as follows:

1. Approximate I_0 from the scaled solar spectrum and the average albedo curve (figure 3.2.3.1 and 3.2.3.2).
2. Calculate $-\ln(I/I_0)$.
3. Filter $-\ln(I/I_0)$ results by procedures described in previous section.
4. Filter the absorption cross section by the same procedure.
5. Perform MLR per equation 3.2.3.4 to obtain column densities.

After the initial column density computation, the absorption contribution by a species may be removed by multiplying the column density value by the absorption cross section and subtracting from the ratio data. This technique is employed in the inversion algorithm prior to iterating steps 2 through 5 above using a different set of filters. Figure 3.2.3.4 shows the results of O_3 column density calculation before and after iteration. Figure 3.2.3.5 shows OCIO errors derived using a simulated lunar event.

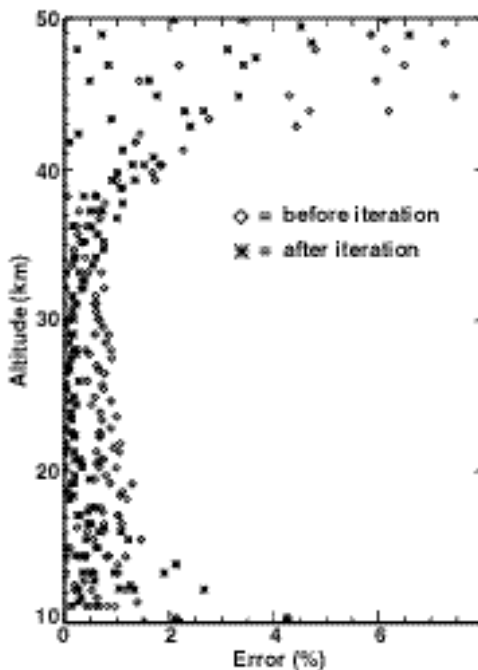


Figure 3.2.3.4 O_3 profile absolute error before and after iteration.

Reduction of Slant Column Densities to Vertical Profiles.

The final stage of the inversion process consists of the reduction of slant path column molecular densities to vertical profiles of molecular number densities is performed. This will follow the SAGE II processing method in which a modified Chahine method [Chahine, 1972, Twomey, 1975, Chu *et al.*, 1979, 1989; Chu, 1985] was employed though alternative methods will be examined. With all species transformed to vertical profiles, construction of the data products listed in Table 3.2.2.2 is executed and the data made available for archival. The altitude registration of the lunar data will be accomplished by the process described in Appendix F.

The construction of the slant column density profile for ozone is unique due to the fact that information on ozone comes from two different measurements. Slant column densities are estimated from the 290nm extinction measurements at high altitude. The slant column profiles will be combined in to a single profile covering the entire range which will then be inverted to a single ozone density profile. The combination procedure will be based on error estimates from each type of slant column estimation and appropriate quality flags will be set indicating the primary source of information at each altitude.

For species which have a significant diurnal variation across the terminator, the assumption of inhomogeneous spherical shells is incorrect. Nevertheless, the assumption will be maintained for the inversion process. In addition, the slant column density profile will be archived for those users wishing to model in detail the variations along the line of sight with heterogeneous photochemical trajectory models.

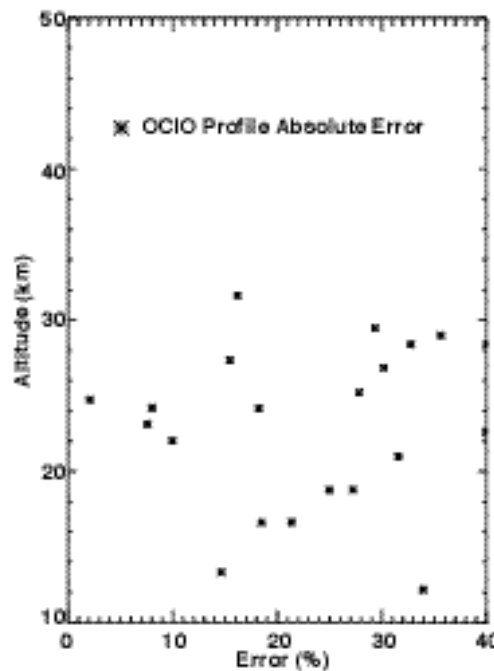


Figure 3.2.3.5 *Simulation of a multi-channel chlorine dioxide measurement from lunar occultation measurements (forward simulation model).*

3.3 Algorithm Testing Requirements

Algorithm testing will be performed both prior to launch and during the lifetime of the instrument using the SAGE III data simulator. The data simulator models both a ray tracing-based model of the atmosphere and accounts for measured and modeled instrument performance. For instance, the instrument model includes the effects of uncertainties in the instrument wavelength-band pass, fields of view, detector response, and spacecraft telemetry. The atmospheric model can include realistic uncertainties in errors in external data sets (e.g., molecular spectroscopy and lunar albedo) and the effects of atmospheric spatial inhomogeneity. The simulator should (and has) helped us to identify software errors and below standard performance in individual retrieval components. The simulator is maintained under configuration control and is considered an adjunct component of the primary operational software.

3.4 Validation Plan

Planning for the validation of all SAGE III data products is covered in the SAGE III Validation Plan (LARC475-00-020). Validation plans are uncertain due to the slip in SAGE

III/Meteor-3M launch date and that document will be revised as launch date and available funds available for validation become more certain.

3.5 Quality Control and Diagnostics

Routine processing will generate a series of quality indicators that assess the quality of the data products and the degree to which the processing of each event was completed according to expectation. The details of this process are outlined in The SAGE III Data Management System Quality Assurance Document (LaRC475-03-115).

4.0 References

- Anderson, J. G., W. H. Brune, S. A. Lloyd, and D. W. Toohey, Kinetics of O₃ destruction by ClO and BrO within the Antarctic vortex: An analysis based on in situ ER-2 data, *J. Geophys. Res.*, 94, 11,480-11,520, 1989.
- Anderson, S. M., J. Morton, and K. Mauersberger, Near-infrared absorption spectra of ¹⁶O₃ and ¹⁸O₃: Adiabatic energy of the ¹A₂ state?, *J. Chem. Phys.*, 94, 6351-6357, 1991.
- Barrett, J. W., P. M. Solomon, R. L. d. Zafra, M. Jaramillo, L. Emmons, and A. Parrish, Formation of the Antarctic ozone hole by the ClO dimer mechanism, *Nature*, 336, 455-458, 1988.
- Baumert, T., J. L. Herek, and A. H. Zewail, Femtosecond real-time probing of reactions. XI. The elementary OClO fragmentation, *J. Chem. Phys.*, 99, 4430-4440, 1993.
- Bishenden, E., and D. J. Donaldson, Mode-specific chemical branching ratios in the photodissociation of OClO, *J. Chem. Phys.*, 99, 3129-3132, 1993.
- Brogniez, C., and J. Lenoble, Size distribution of stratospheric aerosol from SAGE II multi-wavelength extinctions.- in *Aerosols and Climate*, edited by P. V. Hobbs and M. P. McCormick, Editors, pp. 305-311, A. Deepak Publishing, 1988.
- Brown, L. A., V. Vaida, D. R. Hanson, J. D. Graham, and J. T. Roberts, The uptake of chlorine dioxide by model PSCs under stratospheric conditions, *J. Phys. Chem.*, 100, 3121-3125, 1996.
- Buglia, J. J., Compilation of methods in orbital mechanics and solar geometry, *NASA RP 1204*, 1988.
- Buglia, J. J., Effects of ephemeris errors on the accuracy of the computation of the tangent point altitude of a solar scanning ray as measured by the SAGE I-II instrument, *NASA TP-2866*, 1989.
- Chahine, M. T., A general relaxation method for inverse solution of the full radiative transfer equation, *J. Atmos. Sci.*, 29, 741-747, 1972.
- Chu, W., and M. P. McCormick, Inversion of stratospheric aerosol and gaseous constituents from spacecraft solar extinction data in the 0.38-1.0 micron wavelength region, *Appl. Opt.*, 18, 1404-1414, 1979.
- Chu, W. Calculation of atmospheric refraction for space craft remote sensing applications, *Appl. Opt.*, 22, 721-726, 1983.

- Chu, W. P., Convergence of Chahine's nonlinear relaxation inversion method used for limb viewing remote sensing, *Appl. Opt.*, 24, 445-447, 1985.
- Chu, W. P., M. P. McCormick, J. Lenoble, C. Brogniez, and P. Pruvost, SAGE II inversion algorithm, *J. Geophys. Res.*, 94, 8339-8351, 1989.
- Chu, W. P., E. W. Chiou, J. C. Larsen, L. W. Thomason, D. Rind, J. J. Buglia, S. Oltmans, M. P. McCormick, and L. M. McMaster, Algorithms and sensitivity analyses for Stratospheric Aerosol and Gas Experiment II water vapor retrieval, *J. Geophys. Res.*, 98, 4857-4866, 1993.
- Cunnold, D. M., W. P. Chu, R. A. Barnes, M. P. McCormick, and R. E. Veiga, Validation of SAGE II ozone measurements, *J. Geophys. Res.*, 94, 8339-8352, 1989.
- Davis, H. F., and Y. T. Lee, Dynamics and mode specificity in OCIO photodissociation, *J. Phys. Chem.*, 96, 5681-5684, 1992.
- DeMore, W. B., S. P. Sander, D. M. Golden, R. F. Hampson, M. J. Kurylo, C. J. Howard, A. R. Ravishankara, C. E. Kolb, and M. J. Molina, *Chemical Kinetics and Photochemical Data for Use in Stratospheric Modeling, Evaluation number 11*, JPL Publication 94-26, Jet Propulsion Laboratory, Pasadena, CA, 1994.
- Dunn, R. C., J. L. Anderson, C. S. Foote, and J. D. Simon, Solution photochemistry of chlorine dioxide: Mechanisms for the Generation of Atomic Chlorine, *J. Am. Chem. Soc.*, 115, 5307-5309, 1993.
- Dunn, R. C., B. N. Flanders, and J. D. Simon, Solvent effects on the spectroscopy and ultrafast photochemistry of chlorine dioxide, *J. Phys. Chem.*, 99, 7360-7370, 1995.
- Dunn, R. C., and J. D. Simon, Excited-state photoreactions of chlorine dioxide in water, *J. Am. Chem. Soc.*, 114, 4856-4860, 1992.
- Fiedl, R. R., and S. P. Sander, Kinetics and product studies of the reaction $\text{ClO} + \text{BrO}$ using discharge-flow mass spectrometry, *J. Phys. Chem.*, 93, 4756-4764, 1989.
- Gole, J. L., Photochemical isomerization of ClO_2 and the low-lying electronic state of the asymmetric isomer. Possible implications for matrix isolation spectroscopy, *J. Phys. Chem.*, 84, 1333-1340, 1980.
- Gordley, L. L., and J. M. Russell, A fast and accurate radiance algorithm for applications to inversion of limb measurements, in *Remote Sensing of Atmospheres and Oceans*, edited by A. Deepak, p. 591, Academic Press, San Diego, Calif., 1980.
- Graham, J. D., J. T. Roberts, L. A. Brown, and V. Vaida, The uptake of chlorine dioxide by model polar stratospheric cloud surfaces: ultrahigh vacuum studies, *J. Phys. Chem.*, 100, 3115-3120, 1996.

- Hanson, D. R., and A. R. Ravishankara, Reactions of halogen species on ice surfaces, in *The Tropospheric Chemistry of Ozone in the Polar Regions*, edited by H. Niki and K. H. Becker, pp. 281-290, Springer-Verlag, Berlin, 1993.
- Hanson, D. R., and A. R. Ravishankara, Reactive uptake of ClONO_2 on sulfuric acid due to reaction of HCl and H_2O , *J. Phys. Chem.*, **98**, 5728-5735, 1994.
- Hanson, D. R., and A. R. Ravishankara, Heterogeneous chemistry of Bromine species in sulfuric acid under stratospheric conditions, *Geophys. Res. Lett.*, **22**, 385-388, 1995.
- Hanson, D. R., A. R. Ravishankara, and S. Solomon, Heterogeneous reactions in sulfuric acid aerosols: A framework for model calculations, *J. Geophys. Res.*, **99**, 3615-3629, 1994.
- Jafri, J. A., I. B. H. Lengsfeld, J. C. W. Bauschlicher, and D. H. Phillips, The lower electronic states of ClOO : A computational investigation, *J. Chem. Phys.*, **83**, 1693-1701, 1985.
- Jones, R. L., J. Austin, D. S. McKenna, J. G. Anderson, D. W. Fahey, C. B. Farmer, L. E. Heidt, K. K. Kelly, D. M. Murphy, M. H. Proffitt, A. F. Tuck, and J. F. Vedder, Langrangian photochemical modeling studies of the 1987 Antarctic spring vortex-1. Comparison with AAOE observations, *J. Geophys. Res.*, **94**, 11,529-11,558, 1989.
- Kirchhoff, H., On a new proposition in the theory of heat, *Phil. Mag.*, **21**, 240, 1860.
- Kreher K., J. G. Keys, P. V. Johnston, U. Platt, and X. Liu, Ground-based measurements of OCIO and HCl in austral spring 1993 at Arrival Heights, Antarctica, *Geophys Res. Lett.*, **23**, 1545-1548, 1996.
- Lawrence, W. G., K. C. Clemitshaw, and V. A. Apkarian, On the relevance of OCIO photodissociation to the destruction of stratospheric ozone, *J. Geophys. Res.*, **95**, 18,591-18,595, 1990.
- Lanzendorf, E. J. and A. C. Kummel, Photodissociation of condensed films of chlorine dioxide, *Geophys. Res. Lett.*, **23**, 1521-1524, 1996.
- Mauldin, L. E., Stratospheric Aerosol and Gas Experiment II instrument: a functional description, *Opt. Eng.*, **24**, 307-312, 1985.
- Mauldin, L. E., M. P. McCormick, L. R. McMaster, and W. R. Vaughn, The Stratospheric Aerosol and Gas Experiment II (SAGE II) design and in-orbit performance proceeding, Proceedings of SPIE - Instrumentation for Optical Remote Sensing from Space, 589, 104-111, 1985.

- Mauldin, L. E., M. P. McCormick, J. M. Zawodny, L. R. McMaster, W. P. Chu, J. C. Gustafson, and G. L. Maddrea, The Stratospheric Aerosol and Gas Experiment III instrument proposed for EOS: a conceptual design, Int. Congress on Opt. Sci. and Eng. - Paris, France, 1989.
- McCormick, M. P., P. Hamill, T. J. Pepin, W. P. Chu, T. J. Swissler, and L. R. McMaster, Satellite studies of the stratospheric aerosol, *Bull. of the Amer. Met. Soc.*, 60, 9, 1979.
- McCormick, M. P., W. P. Chu, G. W. Grams, P. Hamill, B. M. Herman, L. R. McMaster, T. J. Pepin, P. B. Russell, H. M. Steele, and T. J. Swissler, High-latitude stratospheric aerosol measured by SAM II satellite system in 1978-1979, *Science*, 214, 328-331, October, 1981.
- McCormick, M. P., H. M. Steele, P. Hamill, W. P. Chu, T. J. Swissler, Polar stratospheric cloud sightings by SAM II, *J. Atmos. Sci.*, 39, 6, 1387, 1982.
- McCormick, M. P., SAGE II: an overview, *Adv. Space Res.*, 7, 219-226, 1987.
- McCormick, M. P., *et al.*, Stratospheric Aerosol and Gas Experiment III (SAGE III) aerosol and trace gas measurements for Earth Observing System (EOS), SPIE Paper No. 1491-16, 1991.
- McCormick, M. P., J. M. Zawodny, W. P. Chu, J. W. Baer, J. Guy, and A. Ray, Stratospheric Aerosol and Gas Experiment III (SAGE III), SPIE International Symposium for Optical Engineering - Orlando, FL, 1993.
- McElroy, M. B., R. J. Salawitch, S. C. Wofsy, and J. A. Logan, Reductions of Antarctic ozone due to synergistic interactions of chlorine and bromine, *Nature*, 321, 759-762, 1986.
- Molina, M. J., T.-L. Tso, L. T. Molina, and F. C.-Y. Wang, Antarctic stratospheric chemistry of chlorine nitrate, hydrogen chloride, and ice: release of active chlorine, *Science*, 238, 1253-1257, 1987.
- Penney, C. M., Study of temperature dependence of the Chappuis band absorption of ozone, NASA Contract. Rep., *NASA CR 158977*, 1979. (Available as NTIS X79-10050 from Natl. Tech. Inf. Serv., Springfield, Va.)
- Pepin, T. J. and M. P. McCormick, Stratospheric Aerosol Measurement Experiment MA-007, *NASA TM X-58173*, February, 1976.
- Perner, D., T. Klüpfel, U. Parchatka, A. Roth, and T. Jørgensen, Ground-based UV-VIS spectroscopy: diurnal OCIO-profiles during January 1990 above Søndre Strømfjord, Greenland, *Geophys. Res. Lett.*, 18, 787-790, 1991.

- Peterson, K. A., and H.-J. Werner, Multireference configuration interaction calculations of the low-lying electronic states of ClO₂, *J. Chem. Phys.*, **96**, 8948-8961, 1992.
- Pinnick, R. G., J. M. Rosen, and D. J. Hofmann, Stratospheric aerosol measurements, III: Optical model calculations, *J. Atmos. Sci.*, **33**, 304-314, 1976.
- Pursell, C. J., J. Conyers, P. Alapat, and R. Parveen, Photochemistry of chlorine dioxide on ice, *J. Chem. Phys.*, **99**, 10433-10437, 1995.
- Richard, E. C., and V. Vaida, The photochemical dynamics of the A ²A₂ state of chlorine dioxide, *J. Chem. Phys.*, **94**, 163-171, 1991.
- Rodriguez, J. M., M. K. W. Ko, and N. D. Sze, Chlorine chemistry in the Antarctic stratosphere: impact of OClO and ClO and implications for observations, *Geophys. Res. Lett.*, **13**, 1292-1295, 1986.
- Rühl, E., A. Jefferson, and V. Vaida, Photodissociation of OClO: REMPI study of primary photofragments, *J. Phys. Chem.*, **94**, 2990-2994, 1990.
- Salawitch, R. J., S. C. Wofsy, and M. B. McElroy, Chemistry of OClO in the Antarctic stratosphere: implications for bromine, *Planet. Space Sci.*, **36**, 213-224, 1988.
- Sander, S. P., and R. R. Friedl, Kinetics and product studies of the reaction ClO + BrO using flash photolysis-ultraviolet absorption, *J. Phys. Chem.*, **93**, 4764-4771, 1989.
- Sander, S. P., R. R. Friedl, and Y. L. Yung, Rate of formation of the ClO dimer in the polar stratosphere: implications for ozone loss, *Science*, **245**, 1095-1098, 1989.
- Sanders, R. W., S. Solomon, M. A. Carroll, and A. L. Schmeltekopf, Visible and near-ultraviolet spectroscopy at McMurdo station, Antarctica-4. overview and daily measurements of NO₂, O₃, and OClO during 1987, *J. Geophys. Res.*, **94**, 11,381-11,391, 1989.
- Sanders, R. W., S. Solomon, J. P. Smith, L. Perliski, H. L. Miller, G. H. Mount, J. G. Keys, and A. L. Schmeltekopf, Visible and near-ultraviolet spectroscopy at McMurdo station, Antarctica-9. Observations of OClO from April to October 1991, *J. Geophys. Res.*, **98**, 7219-7228, 1993.
- Schiller, C., A. Wahner, U. Platt, H.-P. Dorn, J. Callies, and D. H. Ehhalt, Near UV atmospheric absorption measurements of column abundances during Airborne Arctic Stratospheric Expedition, January-February 1989: 2. OClO observations, *Geophys. Res. Lett.*, **17**, 501-504, 1990.
- Solomon, S., R. R. Garcia, F. S. Rowland, and D. J. Wuebbles, On the depletion of Antarctic ozone, *Nature*, **321**, 755-758, 1986.

- Solomon, S., G. H. Mount, R. W. Sanders, R. O. Jakoubek, and A. L. Schmeltekopf, Observations of the nighttime abundance of OCIO in the winter stratosphere above Thule, Greenland, *Science*, 242, 550-555, 1988.
- Solomon, S., G. H. Mount, R. W. Sanders, and A. L. Schmeltekopf, Visible spectroscopy at McMurdo station, Antarctica-2. Observations of OCIO, *J. Geophys. Res.*, 92, 8329-8338, 1987.
- Solomon, S., and R. W. Sanders, Visible and near-ultraviolet spectroscopy at McMurdo station, Antarctica-7. OCIO Diurnal photochemistry and implications for ozone destruction, *J. Geophys. Res.*, 95, 13,807-13,817, 1990.
- Solomon, S., R. W. Sanders, M. A. Carroll, and A. L. Schmeltekopf, Visible and near-ultraviolet spectroscopy at McMurdo station, Antarctica-5. Observations of the diurnal variations of BrO and OCIO, *J. Geophys. Res.*, 94, 11,393-11,403, 1989.
- Twomey, S., On the numerical solution of Fredholm integral equation of the first kind by the inversion of the linear system produced by quadrature, *J. Assoc. Comput. Mach.*, 10, 97-101, 1963.
- Twomey, S., Comparison of constrained linear inversion and an iterative nonlinear algorithm applied to the indirect estimation of particle size distributions, *J. Comput. Phys.*, 18, 188-198, 1975.
- Twomey, S., Introduction to the mathematics of inversion in remote sensing and indirect measurements, Elsevier North-Holland Inc., New York, N. Y., 1977.
- Toohey, D. W., and J. G. Anderson, Formation of $\text{BrCl}(\text{}^3\text{}_{0+})$ in the reaction of BrO with ClO, *J. Phys. Chem.*, 92, 1705-1708, 1988.
- Tung, K.-K., M. K. W. Ko, J. M. Rodriguez, and N. D. Sze, Are Antarctic ozone variations a manifestation of dynamics or chemistry?, *Nature*, 322, 811-814, 1986.
- Turnipseed, A. A., J. W. Birks, and J. G. Calvert, Kinetics and Temperature Dependence of the BrO + ClO Reaction, *J. Phys. Chem.*, 95, 4356-4364, 1991.
- Vaida, V., and J. D. Simon, The Photoreactivity of Chlorine Dioxide, *Science*, 268, 1443-1448, 1995.
- Vaida, V., S. Solomon, E. C. Richard, E. Rühl, and A. Jefferson, Photoisomerization of OCIO: a possible mechanism for polar ozone depletion, *Nature*, 342, 405-408, 1989.
- Wahner, A., R. O. Jakoubek, G. H. Mount, A. R. Ravishankara, and A. L. Schmeltekopf, Remote sensing observations of nighttime OCIO column during the Airborne Antarctic Ozone Experiment, September 8, 1987, *J. Geophys. Res.*, 94, 11,405-11,411, 1989.

Wahner, A., and C. Schiller, Twilight variation of vertical column abundances of OClO and BrO in the North polar region, *J. Geophys. Res.*, 97, 8047-8055, 1992.

Young, A. T., Revised depolarization corrections for atmospheric extinction, *Appl. Opt.*, 19, 3427-3430, 1980.

Appendix A. SAGE III Instrument Description

The design of the SAGE III sensor relies heavily upon the flight proven designs used in the SAM II and SAGE I/II instruments. Specifically, the separate sensor and electronics modules concept from SAGE II is utilized, as are the grommet isolation and contamination door designs. Additionally, the SAGE II pointing system and scan mirror designs are reused, with certain necessary modifications (primarily an attenuator filter) to permit solar and lunar observations with the same detector assembly.

The SAGE III sensor assembly, illustrated in Figure A-1, consists of a sun-tracker, telescope, and grating spectrometer with a CCD detector array; the mass is estimated at 35 kg., a volume of 6000 cm³, with an average power of 60 W and a peak power of 75 W. The two-axis passive sun-tracker, with a scan mirror that scans the instrumental field of view across the solar disk, obtains multiple samples at each altitude, improving the measurement precision. Sunspots are readily detected by scanning, rather than staring at the Sun. A pictorial representation of the scanning pattern as a function of tangent altitude and the corresponding detector output (single wavelength) is illustrated in Figure A-2. The two solid lines denote the position of the top and bottom of the solar disk during a sunrise event as viewed from the spacecraft. The gradual expansion of the vertical sun shape is due to atmospheric refraction. The ordinate denotes the tangent altitude, while the abscissa denotes the event time. During an occultation event, the instrument scans the solar disk as indicated by the dashed line in the figure.

The telescope and spectrometer are illustrated in Figure A-3 and constitute new designs optimized to meet the requirements of lunar occultation measurements. The telescope is a f/4 Dall-Kirkham configured design chosen for its ease of alignment; the speed represents a tradeoff between optimum performance and spectral imaging. The spectrometer is a new design, utilizing a holographic, aberration reduced, grating to provide stigmatic imaging at 440 and 868 nm with 1 nm resolution below 450 nm and 2 nm resolution between 740 and 960 nm. The grating is formed on a spherical substrate with a radius of 152 mm and is imaged through a field flattener and order-sorting filters onto the CCD detector. The grating is utilized in the first positive order with diffraction angles between 8.3 and 17.0 degrees; a ruling of 199 lines per millimeter yields a dispersion of 0.94 to 1.88 nm per pixel in the focal plane (depending on wavelength). Evaluation gratings have been tested and demonstrate near-theoretical first-order efficiencies with very low scattered light properties. The spectrometer has been ray-traced and a Monte Carlo simulation of optical tolerances has been performed which indicates that at the wavelengths of best spectral focus, a FWHM bandpass of less than 1.2 nm per pixel should be achievable.

The detector assembly consists of two elements, a Tektronix 800x10 pixel backside-illuminated, thinned CCD array for the 280 - 1040 nm spectral region and a InGaAs

infrared photodiode (1550 \pm 15 nm) that are spatially co-registered. The 800 elements of the array provide the spectral information, the 10 pixels aligned along the horizontal direction are summed together and can be considered a single long pixel. Practical considerations favor pixel subdivision: large pixels can have a low charge transfer efficiency which can be avoided through subdivision, and secondly reducing the horizontal instantaneous field of view (IFOV) can improve the probability of cloud-free measurements. Consequently, in the solar occultation mode, 3 pixels (0.5x1.5 arcminute IFOV) are used to improve the frequency of penetration of the measurements into the troposphere. In contrast, for the lunar occultation measurements, all 10 pixels are used to collect more light.

In the solar occultation mode, the optical throughput of the instrument (grating efficiency and CCD quantum efficiency) combined with the spectral variation in the solar spectrum produce a wide variation in the rate of charge accumulation in the CCD pixels as a function of wavelength. Optimum performance (signal-to-noise ratio and dynamic range) of the detector is achieved when pixels are operated at or near full well. To obtain full well across the spectral region, a spectral flattening filter was considered to selectively attenuate the spectrum near the middle of the spectral band pass, but was determined to be too difficult to design. Instead, the array has been divided into eight segments that have individually controlled integration times to control the filling of the wells. Each segment is operated at or near full well, and the transitions between segments are chosen to avoid potential science channels. This solution optimizes performance and eliminates an item of significant risk and cost.

The lunar occultation measurements are significantly more complicated than the solar measurements; depending upon phase, the Moon is between one million and ten million times less luminous than the Sun, and the lunar albedo is non-uniform making determination of atmospheric transmission non-trivial. The instrument is designed to compensate for this large change in illumination in part by removing the solar attenuator (a neutral density filter with an attenuation of 100) from the optical path. In addition, the integration time is increased from 0.09-2.2 milliseconds to 62 milliseconds (with a resulting increase in signal of 28 to 500), and the instrumental field of view is increased from 3 pixels to 10 pixels (producing an increase of 3.3 in signal level). The resulting gain increase of 165,000 should permit lunar measurements with a signal-to-noise ratio of 150-300, only a factor of 10-20 times poorer than the solar measurements which implies that the altitude range for the species retrievals will be somewhat reduced in the lunar occultation mode.

The detector package has been modeled and electrical, optical, thermal, and radiation-shielding testing of prototype detectors has been performed. The detector assembly is surrounded by an aluminum radiation shield (nominally 1-inch thick) and is illustrated in Figure A-4. The housing is comprised of a base plate, a lead frame assembly, and an optical field flattener. The lead frame assembly is an insulating rectangle through which

the electrical connections to the detector and a thermoelectric cooler (TEC) pass. The field flattener is a plano-concave sapphire window. The purpose of the field flattener, in addition to providing a window to the sealed CCD package, is to further increase the radius of curvature of the focal field and coincide better with the planar CCD array.

Mounted to the backside of the field flattener are three order-sorting filters that provide the out-of-band rejection of light diffracted towards the focal plane assembly from other grating orders. The CCD is mounted to a TEC that is, in turn, mounted to the base plate heat sink. The CCD is designed with built-in thermistors that are part of an active temperature control system to meet the stability and end-of-life dark current requirements. The detector assembly has been included in the stray light analysis of the spectrometer, which showed that a significant reduction in the amount of scattered light could be achieved by rotating the CCD about its long axis by 11 degrees and eliminating internal reflections within the detector assembly. Also within the detector assembly is the InGaAs photodiode for the 1540 nm channel. This channel lies in the zeroth-order beam and has its band pass determined by a filter in much the same manner as was done with two of the channels in SAGE II. This detector is within the assembly because of the close proximity of the zeroth-order light rays to the end of the CCD array. Prototype detectors have been manufactured and tested for spectral quantum efficiency, dark current versus temperature, full-well capacity, charge transfer efficiency, and linearity. Radiation testing with monoenergetic proton beams of differing total doses have assessed the performance in a radiation environment, and led to models of energetic particle transport and secondary particle production, and an assessment of the shielding requirements for the CCD. In addition, models were developed to describe the observed temperature dependent gain of the field effect transistor preamplifiers on the CCD.

The spectrometer with the CCD array of detectors provides continuous wavelength coverage between 280 and 1040 nm and will permit the measurement of multiple absorption features of each gaseous species and multi-wavelength measurements of broadband extinction by aerosols. In the present configuration, 12 solar channels (80 sub-channels) will be routinely utilized in the solar occultation measurements and 3 channels (340 sub-channels) in the lunar occultation measurements, greatly decreasing the random error in the measurements (precision), and allowing for more accurate modeling of the multi-wavelength aerosol extinction. Included within the instrument band pass is the O₂ A band (around 760 nm) which will permit the retrieval of density and temperature with which the viewing geometry (as a pressure level) can be inferred. This improvement over SAGE II, which relied upon the NOAA gridded analyses, should improve the accuracy of the SAGE III profiles and simplify the comparison with other measurements. Additionally, the linear array of detectors will permit on-orbit wavelength and intensity calibration from observations of the exo-atmospheric solar Fraunhofer spectrum. The continuous spectral calibration, combined with the self-calibrating nature of the occultation technique (ratioing the signal transmitted through the atmosphere to the exo-atmospheric reference signal for each measurement) makes SAGE III ideal for long-term

monitoring of trends in ozone and other gas species, which is a central objective of the EOS program.

The expanded spectral coverage of the SAGE III instrument permits the observation of O_3 in the mesosphere between 65 and 85 km by utilizing the UV absorption in the short wavelength region between 385 and 290 nm and, combined with a fixed channel InGaAs detector at 1550 nm, should greatly enhance the characterization of multi-wavelength aerosol and clouds and extend this capability to lower altitudes in the troposphere. The CCD array will provide approximately 2-nm resolution in the spectral region between 920 and 960 nm. In combination with an increase in digitization from 12 bit precision to 16 bit precision, this should allow for greater discrimination of water vapor from aerosol (both volcanic and thin cloud), and better retrieval of the higher water vapor values at lower altitudes in the troposphere than was possible with SAGE II. Table A.1 details the measurement capability of SAGE III for single profile retrievals. The notable difference, as discussed above, is the determination of pressure and temperature from oxygen A band and the improved precision from the inclusion of additional channels.

With a 16-bit A/D converter, the SAGE III spectrometer will allow for variable integration time and on-orbit gain programming necessary for lunar observations. This potentially doubles the number of measurements per orbit, but requires a detector and signal chain that can accommodate the reduced flux observed during lunar occultations. In lunar occultation SAGE III will monitor O_3 , NO_2 , pressure, and H_2O , as well as $OCIO$ and NO_3 .

Table A.1: SAGE III Measurement Capability (single profile)

Channel	Wavelength (nm)	Products	Solar Altitude	Error (%)	Lunar Altitude (km)	Error (%)
S1	290	O ₃	50-85	10	----	----
S2	385	Aerosol	15-40	10	----	----
L1	380-420	OCIO	----	----	15-25	25
S3/L1	433-450	NO ₂ , Aerosol	10-50, 10-40	10 ----	20-50	10
L1	470-490	O ₃	----	----	16-35	10
S4	521	Aerosol, Cloud	6-40	10 ----	----	----
S5	560-616	O ₃	6-60	5	----	----
L1	640-680	NO ₃	----	----	20-55	10
S6	670	Aerosol	3-40	5	----	----
S7	758	Aerosol	3-40	5	----	----
S8/L2	759-771	Pressure, Temperature	0-85, 0-85	2K 2K	6-40 6-40	2 6
S9	869	Aerosol	0-40	5	----	----
S10/L3	933-960	H ₂ O,	0-50,	10	6-25	15
S11	1020	Aerosol, Cloud	0-40	5	----	----
S12	1540	Aerosol, Cloud	0-40	5	----	----

a. Error is estimated precision

b. Lowest altitude is determined by cloud top height

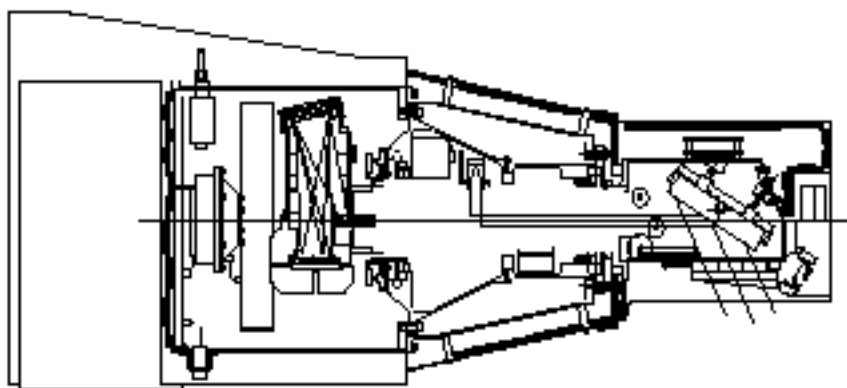


Figure A-1. The SAGE III sensor assembly.

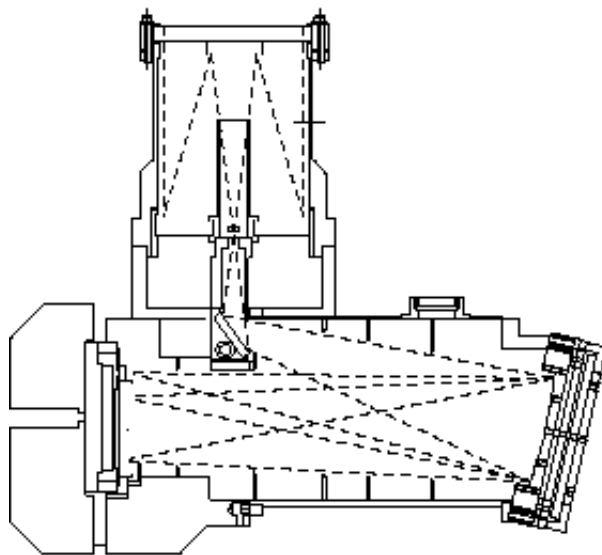


Figure A-2. Optical configuration and ray paths for the SAGE III telescope and spectrometer.

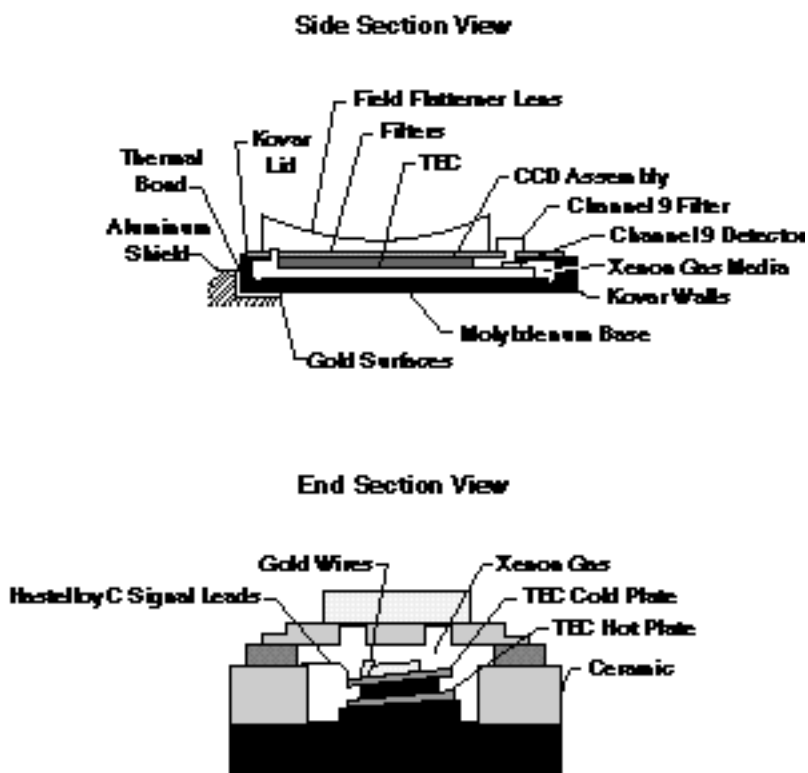


Figure A3. SAGE III detector package.

Appendix B. Implimentation of Atmospheric Retrievals

The retrieval of channels which involve spectroscopic simulation of individual spectral lines employs the technique of Gordley and Russell (1980). This technique involves the precalculation of a grid of transmissions as a function of temperature, pressure and mass path. From the observed atmospheric absorption and an assumed temperature and pressure of a layer, the mass path through a homogenous layer is obtained from precalculated tables. This involves a reverse interpolation in temperature, pressure and mass path within these precalculated tables.

A linear interpolation is not, in general, sufficient. Instead, a second order reverse interpolation is performed by a Taylor series expansion around the closest point in the matrix.

$$\begin{aligned}
 V_{obs} = V_{ijk} &+ \frac{V_{ijk}}{T} (T - T_i) + \frac{V_{ijk}}{p} (p - p_j) + \frac{V_{ijk}}{u} (u - u_k) \\
 &+ \frac{{}^2V_{ijk}}{2T} (T - T_i)^2 + \frac{{}^2V_{ijk}}{2p} (p - p_j)^2 + \frac{{}^2V_{ijk}}{2u} (u - u_k)^2 \times \frac{1}{2} \\
 &+ \frac{{}^2V_{ijk}}{T p} (T - T_i)(p - p_j) + \frac{{}^2V_{ijk}}{T u} (T - T_i)(u - u_k) + \frac{{}^2V_{ijk}}{p u} (p - p_j)(u - u_k)
 \end{aligned} \tag{1}$$

Here V_{obs} is the observed transmission, the transmission at the nearest grid point, i, j and k the indices of the nearest grid point in temperature, pressure and mass path, respectively, T_i, p_j and u_k the temperature, pressure and mass path, respectively, used in the computation of the nearest grid point, and T, p and u the temperature, pressure and mass path corresponding to the observed transmission. All quantities are known except u and this equation forms a quadratic equation in u . Rather than determine the derivatives in this equation by finite differences involving individual transmission values in the precomputed matrix, nine parallel matrices of all of the first and second derivatives in this equation are also precalculated over the same grid. The grid spacings in temperature, pressure and mixing ratio are sufficiently fine that the interpolation from the precalculated derivatives are accurate to within the SAGE III observed uncertainty.

The nine derivatives above are found in a manner analogous to the case of fitting laboratory spectra described by Benner et al. (1995). For N spectral lines the transmission at a specific wavenumber, V , is the product of the transmission of each spectral line, V_i , at that wavenumber.

$$V = \sum_{i=1}^N V_i \quad (2)$$

Differentiating both sides yields an expression for the derivative of the transmission with respect to a parameter, x , which is used in the calculation of the transmission.

$$\frac{V}{x} = \sum_{i=1}^N \frac{V}{V_i} \frac{V_i}{x} \quad (3)$$

This only requires that the derivative with respect to transmission be found for each spectral line individually. An equation may be derived for the second derivatives in a similar manner. The derivative for an individual spectral line is straightforward, although complicated at times. For example, SAGE III uses only Voigt spectral line shapes. The n th derivative for a Voigt spectral line with respect to the mass path, u , can be expressed in terms of only the transmission itself, the mass path and n .

$$\frac{{}^n V_i}{u^n} = \frac{1n V_i}{u} {}^n V_i \quad (4)$$

This expression provides two of the nine required derivatives. The remaining seven derivatives involve at most only algebraic variations of the physical conditions, the spectral line parameters, the transmission and the real and imaginary parts of the complex error function. The real part of the complex error function is just the Voigt function which was used in the calculation of the transmission. Calculating both the real and imaginary parts of the complex error function requires less than twice the time required to calculate the real part.

The light falling upon a single pixel of the CCD cannot be treated as monochromatic. The transmission and derivatives must apply over a finite range of wavelength with the appropriate point spread function, (\cdot) , applied. This is approximated by calculations of the transmission and its derivatives at n specific wavelengths and it is assumed that these values are constant over a finite spectral interval,

$i \cdot$

$$Y_{mean} = \frac{\sum_{i=1}^n (Y_i) (\cdot)_i}{\sum_{i=1}^n (\cdot)_i} \quad (b.5)$$

Here Y may represent either the transmittance or one of its derivatives.

The pressure, temperature and/or mass path as a function of position in the atmosphere are retrieved by means of a global least squares solution. The least squares process requires

the derivative of the calculated transmission with respect to each unconstrained parameter at each observed atmospheric point. These derivatives are supplied directly by interpolation in the precomputed derivative matrix. First order interpolation is done using a Taylor series expansion and the tabulated second derivatives. For example, the derivative of the transmission with respect to temperature requires four table lookups for derivatives.

$$\frac{V}{T} = \frac{V_{ijk}}{T} + \frac{{}^2V_{ijk}}{2T}(T - T_i) + \frac{{}^2V_{ijk}}{T p}(p - p_j) + \frac{{}^2V_{ijk}}{T u}(u - u_k) \quad (6)$$

The derivative of the transmission with respect to a physical parameter in a given layer is insufficient in itself for the global least squares retrieval. The derivative of the transmission of a ray in the occultation mode with respect to a physical parameter in a specific layer requires that the derivative be propagated in the manner of Gordley and Russell (1980) through the atmosphere. For example, the derivative of the transmission V after the final layer N with respect to parameter x from layer i ($1 \leq i \leq N$) is accomplished with a series of derivatives of the transmission with respect to mass path in the precalculated table.

$$\frac{V_N}{x_i} = \frac{V_i}{x_i} + \sum_{j=i}^{N-1} \frac{(V/u)_{T_{j+1}, p_{j+1}, V_{j+1}}}{(V/u)_{T_{j+1}, p_{j+1}, V_j}} \quad (7)$$

For $i = N$, the derivative is zero.

References

- Benner, D. C., C. P. Rinsland, V. Malathy Devi, M. A. H. Smith and D. Atkins, A multispectrum nonlinear least squares fitting technique, *J. Quant. Spectrosc. Radiat. Transfer*, 53, 705-721, 1995.
- Gordley, L. L., and J. M. Russell, A fast and accurate radiance algorithm for applications to inversion of limb measurements, in *Remote Sensing of Atmospheres and Oceans*, edited by A. Deepak, p. 591, Academic Press, San Diego, Calif., 1980.

Appendix C. Atmospheric Inhomogeneity

The SAGE III inversion algorithm, as do essentially all processing algorithms for limb viewing instruments, assumes that the atmosphere is spherically homogeneous. This is probably a good assumption for most stratospheric constituents but is not always true for cloud and may well be a poor approximation for other constituents in the troposphere. Of all the species measured by SAGE III, cloud is most likely to be affected by its own inhomogeneous nature. Despite this, the current SAGE III algorithm, essentially an extension of that used for SAGE II (Kent et al., 1993), neglects this feature of cloud observations. Simulation studies are in progress that may lead to modifications in the cloud detection algorithm that exploit inhomogeneity as a tool to infer the presence of cloud. Inhomogeneous cloud, whether stratospheric or tropospheric, is likely to degrade the quality of concurrent SAGE III measurements of molecular species and temperature and pressure.

Airborne lidar data, taken on an approximately 8000 km flight path over the tropical Pacific, has been used to simulate high altitude SAGE II cloud measurements and their inversion. These simulations produce cloud extinction values similar in magnitude and distribution to those obtained from SAGE II. They also show the existence of three possible error conditions that result from the inhomogeneous nature of the cloud:

1. The true altitude of a cloud may be higher than that found as a result of the SAGE II inversion. Errors of 1 km or more occurred in ~40% of the data set.
2. The inverted cloud extinction may differ (biased low) from the volume averaged extinction along the horizontal ray path.
3. The presence of non-uniform or isolated cloud patches can result in an apparent negative inverted extinction value just below the cloud. Such values were observed in about one third of the simulations. The present SAGE II inversion scheme (bottom up Twomey-Chahine) suppresses these negative values but compensates by reducing the extinction value just above the offending level.

This work is presently being prepared for publication (Simulation of SAGE II cloud measurements using airborne lidar data, G. S. Kent, D. M. Winker, M. A. Vaughan, P.-H. Wang, and K. M. Skeens, 1996).

SAGE transmission measurements are an amalgamation of several independent scans across the Sun. In the presence of cloud or other inhomogeneities, these scans will measure different amounts of transmitted radiation from the same point on the Sun (because the spacecraft moves and the LOS at a given tangent altitude, as a result, also moves). These differences are manifested in the transmission data as an increased standard deviation relative to homogeneous conditions. The possibility exists that this variability may be used as an additional input to the cloud detection algorithm. The simulation described above has

been extended to include spacecraft motion and compared to results from SAGE II observations.

Figure E.1 shows a scatter plot of SAGE II data at an altitude of 14.5 km in which the relative error in the slant path optical depth (SPOD) has been plotted against the SPOD itself. Low values of SPOD, corresponding to cloud-free observations, show low relative error. As cloud is observed in some scans, the relative error increases to a maximum as SPOD also increases. Then as more and more scans observe cloud, the relative error decreases as SPOD continues to increase. Figure E.2 shows the equivalent simulation using airborne lidar data. The behavior is very similar to that shown in Figure E.1. Individual data points in this figure are color coded by their wavelength extinction ratio (525 to 1020 nm aerosol extinction ratio). This ratio is used as the primary discriminator between cloud and aerosol in SAGE II observations and is similar to that proposed for the SAGE III algorithm. We note that the majority of the high error cases (mixed cloud) would be identified as cloud due to their low extinction ratio. However, some high error cases have higher extinction ratios and would not be identified as cloud by the SAGE II algorithm though cloud is clearly present.

Based on these results, we plan to carry out further simulations of the effect of cloud and other inhomogeneities on the inversion algorithm and data quality (not only on cloud presence but also for all other detected species). In particular, we will investigate the effects of PSCs on data from the SAGE III/METEOR 3M flight. The outcome of further simulations may lead to modifications of the inversion algorithm (particularly for cloud detection) and error estimation. We will also consider the implication of cloud homogeneity on the SAGE III validation program (particularly its tropospheric section).

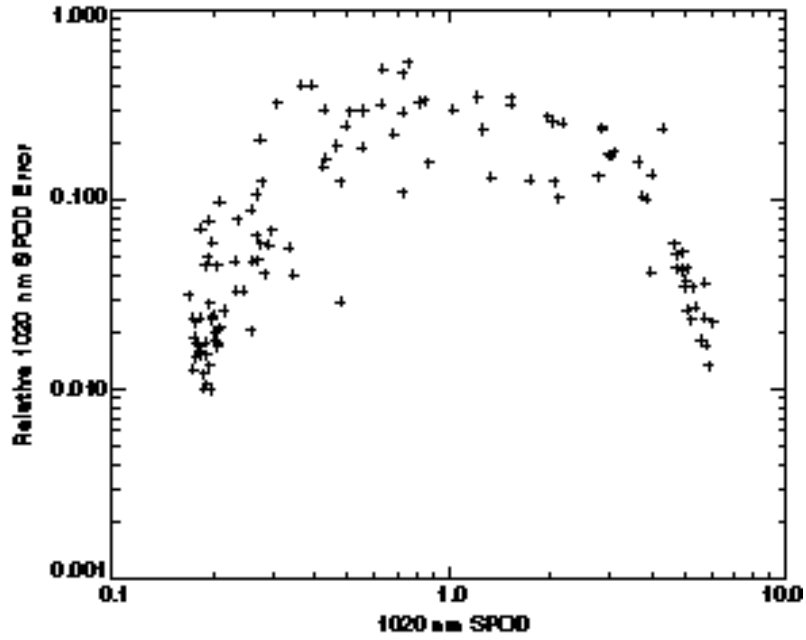


Figure C-1 A scatter plot of SAGE II data at an altitude of 14.5 km, in which the relative error in the slant path optical depth (SPOD) is plotted against the SPOD itself. Data points cover both cloudy and non-cloudy situations.

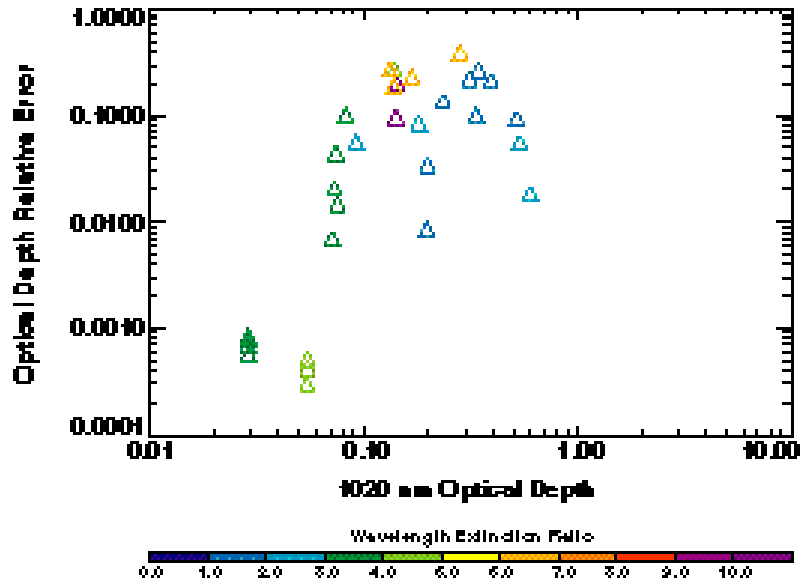


Figure C-2 Scatter plot equivalent to that shown in figure E.1, but derived from simulations based on airborne lidar data obtained within a cloud field. The color coding shows the retrieved 525 to 1020-nm aerosol extinction ratio.

Appendix D. Molecular Absorption Cross-Sections: Spectroscopic Considerations for SAGE III

D.1 Introduction

This appendix reviews the current knowledge of molecular absorption cross sections as it pertains to the SAGE III [Stratospheric Aerosol & Gas Experiment] instrument, and is focused on the spectroscopic needs of the planned SAGE III measurements. This means the discussion is limited to those molecules and spectral regions that will be measured by the SAGE III instrument. Each of the individual molecules measured by SAGE III is discussed in a separate sections. However, each section addresses not only that part of the spectrum which is used to measure that gas but the rest of the spectrum where absorption by that species could interfere with the retrieval of other molecules.

D.2 Species Specific Information

D.2.1 Ozone

D.2.1.1 Ultraviolet

The compilation of UV ozone cross-sections for LOWTRAN 7 and MODTRAN, by G.P. Anderson et al. (1989) is currently recommended, at least for wavelengths up to 345 nm. This compilation is primarily based on the data of Bass & Paur (1985) from 240 to 330, including a quadratic temperature dependence. Between 180 and 240 nm the measurements of Molina & Molina (1986) are used. The measurements of Molina & Molina (1986) and Yoshino et al. (1988) were used to extend the temperature dependent range to 340 nm, and preliminary data of Cacciani et al. (1987), [later published as Cacciani et al. (1989)], was to extend the wavelength coverage to 365 nm.

For wavelengths from 345 to 354 nm, the room temperature values in MODTRAN are consistent with those of Molina & Molina (1986) and with those of Cacciani et al. (1989). However there appears to be a problem with their temperature dependence for wavelengths greater than 345, resulting in a significant underestimate of the ozone absorption at stratospheric temperatures. The cause of this problem with the temperature dependence is not clear, [G.P. Anderson, private communication, 1996].

The recent room temperature measurements by Daumont et al. (1992) from 195 to 345 nm, agree within the stated accuracies with these earlier values. This group recently has extended these measurements to lower temperatures, [Malicet et al., 1998]. Burrows et al. (1999) have also measured the temperature dependence of ozone from 231 to 794 nm. These measurements, along with the recent accurate measurements of the ozone cross section for the 253.7 nm mercury line, by the University of Minnesota Group

[Mauersberger, et al. (1986 & 1987) and Barnes & Mauersberger, (1986)], should be used to re-examine the cross sections for this whole spectral region. The cross section at this mercury line based on Hearn's (1961) data was used to normalize the Bass & Paur (1985) data, along with a number of the earlier measurements.

Brion et al., [1998] have preliminary results continuing the room temperature measurements for ozone absorption from 345 nm to 830 nm. . These should be used to extend the ozone cross sections through the gap that currently exists in the available quantitative data between 360 and 410 nm.

The uncertainties in the UV data are generally within 1 to 2 % for wavelengths less than 325 nm. At longer wavelengths the uncertainties become increasingly larger as the values of the absorption cross section become smaller with increasing wavelength, and the uncertainties in the zero-absorption reference value become more significant. The uncertainties are nearly 10% by 345 nm, and greater than 20% for wavelengths greater than 350 nm. In the vicinity of the absorption minimum near the SAGE 385 nm aerosol channel, the uncertainties in the absorption cross section exceeds a factor of 2. However, at this wavelength the ozone absorption is negligible compared to the aerosol attenuation and is less than 5% of the typical aerosol extinction near 30 km (and the peak ozone mixing ratio).

D.2.1.2 Visible and Near Infrared Cross-Sections:

Recently there have been a several new spectroscopic studies of the ozone Chappuis and Wulf absorption bands, (S.M.Anderson et al., 1990, 1991,1993a, and Burkholder & Talukdar, 1994) along with measurements of the absolute cross-section at selected wavelengths near the peak of the Chappuis band, (Anderson & Mauersberger, 1992), and in the near IR, (S.M.Anderson et al., 1993b). Shettle & Anderson (1994) have used these to develop a new set of room temperature ozone absorption cross-sections. They normalized the spectral measurements to agree with the absolute cross-section data, within the measurement uncertainties, and smoothly joined the different sets of measurements, to provide the new cross-section over the spectral range from 407 to 1089 nm.

The accuracy of this data set is about 1 to 2% from about 520 nm through 800 nm, where they can be constrained by the measurements of Anderson & Mauersberger, (1992), and of S.M.Anderson et al., (1993b). At the extreme wavelengths near 407 and 1089 nm, where the cross section becomes very small the uncertainties are driven by sensitivity of the measurements and possible errors in the zero absorption reference value. Near these wavelengths the uncertainties in the data can exceed 25%, decreasing to 10% near 450 nm and to less than 5% near 500 nm. At the longer wavelengths, the uncertainties in the ozone cross sections increase from 2% to 5% between 800 and 850 nm, with a further increase to

about 10% near 950 nm. The recent results of Brion et al. [1998], tend to be systematically higher by 1% than the measurements discussed above.

Burkholder & Talukdar (1994) have provided a very nice measurement of the temperature dependence of the Chappuis band [from 407 to 762 nm], where they use two identical cells to directly measure the ratio of the cross sections at 298 K and a reduced temperature between 220 and 280 K.

The most significant deficiencies in the ozone data for SAGE III are the need to extend the measurements of the temperature dependence to 180 K, to cover the full range of stratospheric temperatures and through the near IR. The latter is needed more to remove ozone as an interfering species from the SAGE measurement of aerosols and water vapor in the near IR as directly to measure ozone. While Burrows et al. (1999) have measured the temperature dependence in out to 794 nm, their room temperature data is systematically higher than either the Shettle & Anderson (1994) compilation or the Brion et al. (1998) measurements throughout the visible. These differences range from 3 to 5 % near the 600 nm Chappuis peak, to in excess of 20% near 750 nm. Also the Burrows et al. (1998) temperature dependence in the visible shows internal inconsistencies.

D.2.1.3 References

Anderson, G.P., F.X.Kneizys, E.P.Shettle, L.W.Abreu, J.H.Chetwynd, R.E.Huffman, & L.A.Hall (1989), "UV Spectral Simulations Using LOWTRAN 7", in *Atmospheric Propagation in the UV, Visible, IR, & MM-Wave Region and Related Systems Aspects*, AGARD Conference Proceedings No. 454, Proceedings of the AGARD Electromagnetic Wave Propagation Panel Symposium Copenhagen, Denmark, 9-13 October 1989.

Anderson, S.M., P. Hupalo, and K. Mauersberger, "Rotational structure in the near-infrared absorption spectrum of ozone", *J. Chem. Phys.*, 99, 737-739, 1993a.

Anderson, S.M., P. Hupalo, and K. Mauersberger, "Ozone absorption cross section measurements in the Wulf bands", *Geophys. Res. Lett.*, 20, 1579-582, 1993b.

Anderson, S.M., J. Maeder, and K. Mauersberger, "Effect of isotopic substitution on the visible absorption spectrum of ozone", *J. Chem. Phys.*, 94, 6351-6357, 1991.

Anderson, S.M. and K. Mauersberger, "Laser measurements of ozone absorption cross sections in the Chappuis band", *Geophys. Res. Lett.*, 19, 933-936, 1992.

- Anderson, S.M., J. Morton, and K. Mauersberger, "Near-infrared absorption spectra of $^{16}\text{O}_3$ and $^{18}\text{O}_3$: Adiabatic energy of the $^1\text{A}_2$ state?", *J. Chem. Phys.*, 93, 3826-3832, 1990.
- Barnes, J. & K. Mauersberger (1987), "Temperature Dependence of the Ozone Absorption Cross Section at the 253.7-nm Mercury Line", *J. Geophys. Res.*, 92, 14,861-14,864.
- Bass, A.M. and R.J.Paur (1985), "The ultraviolet Cross-Sections of Ozone. I. Measurements in Atmospheric Ozone", *Proceedings of the Quadrennial Ozone Symposium in Halikidi, Greece*, ed. by C.Zeferos and A.Ghaz, pp 606-616.
- Brion, J. A. Chakir, J. Charbonnier, D. Daumont, C. Parisee, J. Malicet (1998), "Absorption Spectra Measurements for the Ozone Molecule in the 350 to 830 nm Region", *J. Atmos. Chem.*, 30, 291-299.
- Burkholder, J.B. and R.K. Talukdar, "Temperature dependence of the ozone absorption spectrum over the wavelength range 410 to 760 nm", *Geophys. Res. Lett.*, 21, 581-584, 1994.
- Burrows, J.P., A. Richter, A. Dehn, B. Deters, S. Himmelmann, S. Voigt, and J. Orphal, (1999), "Atmospheric remote-sensing reference data from GOME – 2. Temperature-dependent absorption cross sections of O_3 in the 231-794 nm range", *J. Quant. Spectrosc. Radiat. Transfer*, 61, 509-517.
- Cacciani, M., A.diSarra, and G.Fiocco, (1987), "Laboratory Measurements of the Ozone Absorption Coefficients in the Wavelength Region 339-362 nm at Different Temperatures", Dept. of Physics, University of Roma - La Sapienza, Italy, Internal Note No. 882.
- Cacciani, M., A.diSarra, and G.Fiocco, and A.Amuruso, (1989), "Absolute Determination of the Cross-Sections of Ozone in the Wavelength Region 339-355nm at Temperatures 220-293K", *J. Geophys. Res.*, 94, 8485-8490.
- Daumont, D., J.Brion, J.Charbonnier, & J.Malicet, (1992), "Ozone UV Spectroscopy I: Absorption Cross Sections at Room Temperature", *J. Atmos. Chem.*, 15, 145-155.
- Malicet, J., D. Daumont, J. Charbonnier, C. Parisse, A. Chakir, and J. Brion (1995) "Ozone UV spectroscopy. II Absorption cross-sections and temperature dependence", *J. Atmos. Chem.*, **21**, 263-273.
- Mauersberger, K., J.Barnes, D.Hanson, & J. Morton, (1986), "Measurement of the Ozone Absorption Cross Section at the 253.7 Mercury Line", *Geophys. Res. Lett.*, 13, 671-673.

Mauersberger, K., D.Hanson, J.Barnes, & J. Morton, (1987), "Ozone Vapor Pressure and Absorption Cross Section Measurements: Introduction of an Ozone Standard", *J. Geophys. Res.*, 92, 8480-8485.

Molina, L.T. and M.J.Molina (1986) "Absolute Absorption Cross Sections of Ozone in the 185-350 nm Wavelength Range", *J. Geophys. Res.*, 91, 14,501-14,509.

Shettle, E.P. & S.M.Anderson, (1994), "New Visible and Near IR Ozone Cross Sections for MODTRAN", presented at the 17th Annual Review Conference on Atmospheric Transmission Models, Phillips Laboratory, Bedford, MA 7-8 June 1994.

Yoshino, K. D.E.Freeman, J.R.Esmond, and W.H.Parkinson, (1988) "Absolute Absorption Cross Section Measurements of Ozone in the Wavelength Region 238-335 nm and the Temperature Dependence", *Planet. Space Sci.*, 36, 395-398.

D.2.2 Nitrogen Dioxide

SAGE II has used the NO₂ cross sections measured by Graham & Johnston (1974) and compiled by Goldman et al. (1978) for their retrieval of the NO₂ profiles, (Cunnold et al., 1991). Since then there have been several new measurements of NO₂ absorption cross sections, [Schneider et al., 1987; Davidson et al., 1989; Amoruso et al., 1993; Harwood and Jones, 1994; Mérienne et al., 1995; and Coquart et al., 1995]. Unfortunately intercomparisons of these different data sets with each other and the Graham & Johnston (1974) measurements show differences as large as 1 nm in the position of the minima and maxima of the absorption as a function of wavelength, in addition to differences of up to 10-20 % in the total cross section. One deficiencies of many of these measurements (and most of the earlier ones) is they were made at resolutions of 0.5 to 2 nm which is too coarse to resolve the structure present in the absorption spectrum. Kirmse, et al. (1997) have concatenated several of these earlier measurements to develop a single NO₂ cross section covering 300 to 908 nm. Using the Mérienne et al. (1995) for the 300 to 500 nm region which includes the 420 to 460 nm region used by SAGE III for its NO₂ measurements.

Harder et al. [1997], provide a detailed critical evaluation of the earlier measurements, in addition to high spectral resolution [< 0.01 nm] data of their own, covering 350 to 585 nm, at temperatures between 217 and 298 K. These agree with the University of Reims data to about 4% in absolute cross section. The details of the spectral structure agree although the effects of the aliasing in the Reims data are clearly present.

Recently Yoshino et al. (1997) and Vandaele, et al. (1996 and 1998) have also made high spectral resolution (< 0.1 nm) measurements of the NO₂ cross sections. These all show

agree with the high resolution data of Mérienne et al. (1995) and Harder et al. (1997), to 3 to 5 %. Most of these results include at least one low temperature measurement (except Yoshino et al., 1997). These low temperature measurement also agree to within 5%, with the spectral variations becoming more pronounced. That is the local minima decrease with decreasing temperature and the local maxima increasing with decreasing temperature.

With an instrument such as SAGE II which uses the difference between a single minimum and maximum, the use of a pair where there are large differences between the positions and cross sections, could lead to errors as large as 50 % by using the wrong cross section data. It should be noted that the validation of the SAGE II NO₂ measurements, [Cunnold et al., 1991], indicate that the SAGE NO₂ data is accurate to 15%. SAGE III will retrieve the NO₂ from the structure across several minima and maxima, which should mean it is much less sensitive to the position and cross sections of individual pairs of the minima and maxima. In fact the SAGE III spectral measurements can be used to check for systematic wavelength shifts in the NO₂ absorption data used in the algorithm.

In the spectral region from 400 nm to 460 nm, where there are a number of good quality high resolution measurements available, the uncertainties in the NO₂ absorption cross sections are 3-5 %. This includes the portion of the spectrum used by SAGE III and many other instruments to determine the concentration of NO₂ in the atmosphere. From 300 nm to 400 nm and from 460 nm to 500 nm the uncertainties are 5-7 %. At longer wavelengths, which are still important to remove the contributions of NO₂ from the measurements of other species such as aerosols or NO₃, the uncertainties are 5-10 %, and are limited to measurements with resolutions (and wavelength accuracies) of 0.5 to 2 nm, which means additional errors will be introduced in convolving them with the spectral response of the SAGE III instrument. The greatest needs for additional measurements are for high resolution data at wavelengths longer than 500 nm and for low temperature measurements at all wavelengths down to 180 K, to cover the full range of stratospheric temperatures.

D.2.2.1 References

- Amoruso, A.L., G.Crescentini, G.Fiocco, and M.Volpe, (1993) "New Measurements of the NO₂ Absorption Cross Section in the 440- to 460- nm region and estimates of the NO₂ - N₂O₄ Equilibrium Constant", *J. Geophys. Res.*, 98, 16,857-16,863.
- Bass, A.M., A.E.Ledford Jr., and A.H.Laufer, "Extinction Coefficients of NO₂ and N₂O₄", *J. Res. Natl. Bur. Stand.*, 80A, 143-166.
- Coquart, B. A.Jenouvrier, and M.F.Mérienne (1995) "The NO₂ Absorption Spectrum. II: Absorption Cross-Sections at Low Temperature in the 400-500 nm Region", *J. Atmos. Chem.*, 21, 251-261.

- Cunnold, D.M., J.M.Zwadony, W.P.Chu, J.P.Pommereau, F.Goutail, J.Lenoble, M.P.McCormick, R.E.Viega, D.Murcray, N.Iwagami, K.Shibasaki, P.C.Simon, & W.Peetermans, (1991), "Validation of SAGE II NO₂ Measurements", *J. Geophys. Res.*, 96, 12,913-12,925.
- Davidson, J.A., C.A.Cantell, A.H.McDaniel, R.E.Shetter, S.Madronich, and J.G.Calvert, (1989), "Visible-Ultraviolet Absorption Cross Sections for NO₂ as a Function of Temperature", *J. Geophys. Res.*, 93, 7105-7112.
- Frost, G.J., L.M.Goss, & V.Vaida, (1996) "Measurements of High-Resolution Ultraviolet-Visible absorption Cross Sections at Stratospheric Temperatures: 1. Nitrogen Dioxide", *J. Geophys. Res.*, 101, 3869-3877.
- Graham, R. and H.S.Johnston (1974) "Photochemistry of NO_x and HNO_x Compounds", *Can. J. Chem.*, **52**, 1415-1423. [Values tabulated by A.Goldman, U. of Denver]
- Hall, T.C. and F.E. Blacet, (1952) "Separation of the Absorption Spectra of NO₂ and N₂O₄ in the range 2400-5000 Å", *J. Chem. Phys.*, 20, 1745-1749.
- Harder, J.W., J.W.Brault, P.V.Johnston, & G.H.Mount [1997], "Temperature Dependent NO₂ Cross Sections at High Spectral Resolution", *J. Geophys. Res.*, 102, 3861-3879.
- Harwood, M.H. and R.L.Jones (1994), "Temperature Dependent Ultraviolet-Visible Absorption Cross-Sections of NO₂ and N₂O₄: Low-Temperature Measurements of the Equilibrium Constant for 2NO₂ ⇌ N₂O₄", *J. Geophys. Res.*, 99, 22,955-22,964.
- Mérienne, M.F., A.Jenouvrier, B.Coquart, (1995) "The NO₂ Absorption Spectrum. I: Absorption Cross-Sections at Ambient Temperature in the 300-500 nm Region", *J. Atmos. Chem.*, 20, 281-297.
- Schneider, W.G., G.K.Moortgat, G.S.Tyndall, and J.P.Burrows, (1987), "Absorption Cross Sections of NO₂ in the UV and Visible Region (200-700 nm) at 298 K", *J. Photochem. Photobiol. A Chem.*, 40, 195-217.
- Vandaele, A.C., C.Hermans, P.C.Simon, M.Carleer, R.Colin, S.Fally, M.F.Merienne, A.Jenouvrier, & B.Coquart, (1998) "Measurements of the NO₂ absorption cross-sections from 42,000 cm⁻¹ to 10,000 cm⁻¹ (238-1000 nm) at 220 K and 294 K", *J. Quant. Spectrosc. Radiat. Transfer*, 59, 171-184.
- Yoshino, K., J.R.Esmond, W.H.Parkinson, (1997) "High-resolution absorption cross section measurements of NO₂ in the UV and visible region", *Chem. Phys.*, 221, 169-174.

D.2.3 Oxygen

Accurate knowledge of the oxygen absorption cross sections are critical for the SAGE III Experiment, since the SAGE III oxygen measurements are used to establish the atmospheric density, temperature, and pressure profiles. In addition to the direct scientific need for these profiles, they are also needed to remove the molecular Rayleigh scattering contribution from the measurements of other species at all wavelengths, and for the retrieval of the mixing ratio of the other gaseous species on pressure surfaces. This removes the need for external source of this data, such as the NMC analyses which were used for the SAGE I and II instruments. To retrieve the oxygen density, from which the atmospheric density, temperature, and pressure profiles will be derived, SAGE III will use differential absorption measurements across the oxygen A band from 755 to 775 nm.

The Ritter & Wilkerson (1986) measurements of the oxygen A band with a stated accuracy of about 2%, appear to be the best of the available data. They have been adapted by Chance (1995) for use with the Global Ozone Monitoring Experiment (GOME). However, their band strength is higher than all of the previous measurements that they include in their Table IV, exceeding the next highest by nearly 5%, the mean by 11%, and exceed by 15% the data of Miller et al. (1969), (with a stated accuracy of 4%), which are the basis of the 1992 HITRAN database, (Rothman et al., 1992). Ritter & Wilkerson's (1986) line widths are near the middle of the range of the previous measurements, which have a 30% range of values. However, while the 1996 HITRAN database adapted the Ritter & Wilkerson (1986) line strengths, it continues to utilize the line widths of Givers et al. (1974), which are at the low end of the available measurements.

Recently Brown and Plymate (1999) have measured the oxygen A band. The line positions, line intensities and pressure-broadening coefficients of 44 transitions in the oxygen A-band near 760 nm (from 13040 to 13168 cm^{-1}) have been calibrated using laboratory data recorded at 0.02 cm^{-1} resolution with the Fourier transform spectrometer at Kitt Peak in Arizona. The pressure-broadening coefficients for self- and nitrogen-broadened widths and pressure-induced shifts in line positions have been measured through $J'' = 24$; these have been combined and modeled with a polynomial expressed as a function of the upper state quantum number in order to compute the corresponding air-broadened line shape coefficients associated with Voigt profiles. The temperature dependence of the line widths has been determined from absorption spectra obtained with gas samples temperatures between 205 K and 297 K

The measured intensities demonstrate that the values selected for the 1996 HITRAN database are valid to within 1%. However, the line positions are in error by 0.002 to 0.015 cm^{-1} and the widths by 7 to 20%. Although the individual new measurements of temperature dependence of widths have uncertainties of 15%, the average of new measured values is within 2% of the mean value previously selected by HITRAN.

D.2.3.1 References

- Brown, L.R. and C. Plymate, (1999) "Experimental line parameters of the oxygen A-band at 760 nm.", *submitted to J. Mol. Spectrosc.*
- Brown, L.R. and R.A.Toth (1995) "Laboratory Spectroscopy of SAGE Molecules", Unpublished Manuscript.
- Chance, K., (1995) "O₂ A Band Studies for Cloud Detection and Algorithm Improvement" (1995), Contact Report for ESA.
- Giver, L.P., R.W.Boese, & J.H.Miller (1974) "Intensity Measurements, Self-Broadening Coefficients, and Rotational Intensity Distribution for Lines of the Oxygen B Band at 6880 C", *J. Quant. Spectrosc. Radiat. Transfer*, 14, 793-802.
- Miller, J.H., R.W.Boese, & L.P.Giver (1969) "Intensity Measurements and Rotational Intensity Distribution for the Oxygen A Band", *J. Quant. Spectrosc. Radiat. Transfer*, 9, 1507-1517.
- Newnham, D.A., and J. Ballard (1998) "Visible absorption cross sections and integrated absorption intensities of molecular oxygen (O₂ and O₄)", *J. Geophys. Res.*, 103, 28,801-28,816.
- Ritter, K.J. and T.D.Wilkerson (1987), "High Resolution Spectroscopy of the Oxygen A Band", *J. Molec. Spectrosc.*, 121, 1-19
- Rothman, L.S., R.R.Gamache, R.H.Tipping, C.P.Rinsland, M.A.H.Smith, D.C.Benner, V.M.Devi, J.-M.Flaud, C.Camy-Peyret, A.Perrin, A.Goldman, S.T.Massie, L.R.Brown, & R.A.Toth, (1992) "The HITRAN Molecular Database Editions of 1991 and 1992", *J. Quant. Spectrosc. Radiat. Transfer*, 48, 469-507.
- Rothman, L.S. C.P. Rinsland, A. Goldman, S.T. Massie, D.P. Edwards, J.-M. Flaud, A. Perrin, C. Camy-Peyret, V. Dana, J.-Y. Mandin, J. Schroeder, A. McCann, R.R. Gamache, R.B. Watson, K. Yoshino, K.V. Chance, K.W. Jucks, L.R. Brown, V. Nemtchinov, and P. Varanasi (1998), "The HITRAN molecular spectroscopic database and HAWKS (HITRAN Atmospheric WorkStation): 1996 edition", *J. Quant. Spectrosc. Radiat. Transfer*, 60, 665-710.

D.2.4 Water Vapor

To measure atmospheric water vapor SAGE III will use differential absorption in the near IR water band from 920 to 960 nm. The HITRAN database, Rothman (1992), based on

the measurements of Chevillard et al. (1989), provides the best available spectroscopic data, in this region. This is an improvement over the 1982 edition of the HITRAN database used by Chu et al. (1993) for the water vapor retrievals from SAGE II. However as noted by Brown and Toth (1995), this band is a complex of 10 interacting vibrational states and a complete theoretical modeling has not been accomplished to date, limiting the ability to give a complete accurate listing of the line positions, intensities, and spectral assignments. Recently Giver et al. (1999) have reported that there were systematic errors in implementing the line intensities of water vapor into the HITRAN database, which affects all the visible and near IR water bands with wavelengths less than 1200 nm. For the band centered around 940 nm, which will be by SAGE III to retrieve water vapor, this correction amounts to a 14.4 % increase in all the lines derived from the data of Chevillard et al. (1989). Which applies to most of the lines in this band. There are number of weak lines in this region due to H_2^{17}O and H_2^{18}O , and a few unassigned lines. It is presently not clear whether this correction applies to any of these lines, however altogether they contribute only about 1% of the total band strength.

The reported accuracies of the Chevillard et al. (1989) data are 7 to 50 %, depending on the spectral line. Given the 50 % uncertainties apply to the weakest lines, when integrated over the 2 nm resolution of the SAGE III detector, the water vapor absorption is known to about 10 to 15 %. To achieve greater accuracy for water vapor retrievals will require new measurements of the water vapor spectroscopy in the near IR.

Recently Brown et al. (1999, unpublished manuscript), have obtained new measurements of the water vapor lines for the 940 nm band. The line positions and line intensities of some 2600 transitions have been retrieved from 17 absorption spectra recorded at 0.01 and 0.02 cm^{-1} resolution using the Fourier transform spectrometer at Kitt Peak in Arizona. These have been combined with published analyses for isotopic water ($\text{H}_2\text{-}^{16}\text{O}\text{-}^{18}\text{O}$ and $\text{H}_2\text{-}^{16}\text{O}\text{-}^{17}\text{O}$) to produce a new line list of some 4130 transitions from 9676.8789 to 11386.2119 cm^{-1} . Available air-broadened and self-broadened line widths from other vibrational bands at 6 μm and 2.1 μm have been inserted for A- and B- type transitions of bands in the 0.96 μm region. There are no new data for pressure-shifts and temperature dependences, however.

This study will correct the conversion mistakes recently uncovered in the visible line parameters of water by COMPLETELY REPLACING the current 0.96 μm list in HITRAN and GEISA with better quality measurements (0.001 cm^{-1} for positions and 3% for the intensities). The individual intensities range from 6.5×10^{-22} to $1 \times 10^{-27} \text{ cm}^{-1}/(\text{molecule} \times \text{cm}^2)$ at 296 K.

D.2.4.1 References

- Brown, L.R. and R.A.Toth (1995) "Laboratory Spectroscopy of SAGE Molecules", Unpublished Manuscript.
- Chevillard, J.-P., J.-Y.Mandin, J.-M.Flaud, & C. Camy-Peyret (1989) " H_2^{16}O : Line positions and intensities between 9500 and 11500 cm^{-1} . The interacting vibrational states (041), (220), (121), (022), 9300), (201), (102), and (003)", *Can. J. Phys.*, 67, 1065-1084
- Chu, W.P., E.W.Chiou, J.C.Larsen, L.W.Thomason, D.Rind, J.J.Buglia, S.Oltsman, M.P.McCormick, & L.M.McMaster (1993) "Algorithms and sensitivity analyses for Stratospheric Aerosol and Gas Experiment II water vapor retrieval", *J. Geophys. Res.*, 98, 4857-4866.
- Giver, L.P., C. Chackerian, and P. Varanasi, "Visible and Near-Infrared H_2^{16}O Line Intensity Corrections for HITRAN-96", *to be published in J. Quantat. Spectrosc. Radiative Transf.*, 1999.
- Rothman, L.S., R.R.Gamache, R.H.Tipping, C.P.Rinsland, M.A.H.Smith, D.C.Benner, V.M.Devi, J.-M.Flaud, C.Camy-Peyret, A.Perrin, A.Goldman, S.T.Massie, L.R.Brown, & R.A.Toth, (1992) "The HITRAN Molecular Database Editions of 1991 and 1992", *J. Quant. Spectrosc. Radiat. Transfer*, 48, 469-507.
- Rothman, L.S., R.R.Gamache, A.Barbe, A.Goldman, J.R.Gillis, L.R.Brown, R.A.Toth, J.-M.Flaud, & C.Camy-Peyret (1983) "AFGL atmospheric absorption line parameters compilation: 1982 edition", *Appl. Opt.*, 22, 2247-2256.
- Rothman, L.S. C.P. Rinsland, A. Goldman, S.T. Massie, D.P. Edwards, J.-M. Flaud, A. Perrin, C. Camy-Peyret, V. Dana, J.-Y. Mandin, J. Schroeder, A. McCann, R.R. Gamache, R.B. Watson, K. Yoshino, K.V. Chance, K.W. Jucks, L.R. Brown, V. Nemtchinov, and P. Varanasi (1998), "The HITRAN molecular spectroscopic database and HAWKS (HITRAN Atmospheric WorkStation): 1996 edition", *J. Quant. Spectrosc. Radiat. Transfer*, 60, 665-710.

D.2.5 The Nitrate Free Radical NO_3

SAGE III utilizing differential absorption spectroscopy in the 640 to 680 nm region will measure the nitrate free radical NO_3 . It is at least a weak absorber throughout the visible, although strong absorption features and 623 and 662 nm dominate its visible spectrum. A

general review of the Nitrate Free Radical NO_3 , including its spectroscopy, is given by Wayne et al. (1991)n.

DeMore et al. (1997) recommend using an average of the studies by Marinelli et al. (1982), Ravishankara & Wine (1983), Burrows et al. (1985), Ravishankara & Mauldin (1986), Sander (1986), Canosa-Mas et al. (1987), and Cantrell et al. (1987) for the cross section at the 662 nm peak at room temperature. There is disagreement in the temperature dependence with Cantrell et al. (1987) finding the absorption to be independent of temperature between 215 and 348 K, and Ravishankara & Mauldin (1986) and Sander (1986) reporting the cross section increasing with decreasing temperature. For the cross section increase, Ravishankara & Mauldin report 40 % between 298 and 220 K and Sanders 20 % between 298 and 230 K. The recent measurements of Yokelson et al. (1994) tend to support the temperature dependence of Sanders. Yokelson et al. also note that their measurements can be considered to supersede the earlier results of Ravishankara & Mauldin (1987).

The uncertainties in the absorption cross sections are 10-15 % at room temperature and 20-25 % at stratospheric temperatures. Given this results in a corresponding uncertainty of the retrieved NO_3 amounts, improved measurements are needed.

D.2.5.1 References

Burrows, J.P., G.S.Tyndall, & G.K.Moortgat (1985) "Absorption spectrum of NO_3 and kinetics of the reactions of NO_3 with NO_2 , Cl, and several stable atmospheric species at 298 K", *J. Chem. Phys.*, 89, 4848-4856.

Canosa-Mas, C.E., M.Fowles, P.J.Houghton, & R.P.Wayne (1987) "Absolute absorption cross section measurements on NO_3 ", *J. Chem. Soc. Faraday Trans. II*, 83, 1465-1474.

Cantrell, C.A., J.A.Davidson, R.E.Shetter, B.A.Anderson, & J.G.Calvert (1987) "The temperature Invariance of the NO_3 absorption cross section in the 662 nm region", *J. Phys. Chem.*, 91, 5858-5863.

DeMore, W.B., S.P. Sander, D.M.Golden, R.F.Hampson, M.J.Kurylo, C.J.Howard, A.R.Ravishankara, C.E.Kolb, M.J.Molina (1994), *Chemical Kinetics and Photochemical Data for Use in Stratospheric Modeling Evaluation Number 11*, JPL Publication 94-26

DeMore, W.B., S.P. Sander, D.M.Golden, R.F.Hampson, M.J.Kurylo, C.J.Howard, A.R.Ravishankara, C.E.Kolb, M.J.Molina (1997), *Chemical Kinetics and*

- Marinelli, W.J., D.M.Swanson, & H.S.Johnston (1982) "Absorption cross sections and line shape for the NO₃ (0-0) band", *J. Chem. Phys.*, 76, 2864-2870.
- Ravishankara, A.R. & R.L.Mauldin III (1986) "Temperature dependence of NO₃ cross section in the 662-nm region", *J. Geophys. Res.*, 91, 8709-8712.
- Ravishankara, A.R. & P.H.Wine (1983) "Absorption Cross Sections for NO₃ between 565 and 673 nm", *Chem. Phys. Lettr.*, 101, 73-78.
- Sanders, S.P. (1986) "Temperature dependence of the NO₃ absorption spectrum", *J. Chem. Phys.*, 90, 4135-4142.
- Wayne, R.P., I.Barnes, P.Biggs, J.P.Burrows, C.E.Canosa-Mas, J.Hjorth, G. Le Bras, G.K.Moortgat, D.Perner, G.Poulet, G.Restlli, & H.Sidebottom (1991) "The Nitrate Radical: Physics, Chemistry, and the Atmosphere", *Atmos. Environ.*, 25A, 1-203.
- Yokelson, R.J., J.B. Burkholder, R.W. Fox, R.K. Talukdar, and A.R. Ravishankara, "Temperature Dependence of the NO₃ Absorption Spectrum", *J. Phys. Chem.*, 98, 13,144-150, 1994.

D.2.6 Symmetric Chlorine Dioxide OClO

Symmetric chlorine dioxide, OClO, has series of absorption peaks between 280 and 480 nm, which reach a maximum near 351 nm. The region from 380 to 420 nm will be used for the SAGE III retrievals of OClO. While there have been a number of spectroscopic studies of OClO, relatively few experiments have provided absolute cross sections at room temperature, with apparently only Wahner et al. (1987) examining the temperature dependence. Frost et al. (1996) have recently reported a spectroscopic study of OClO at stratospheric temperatures (200 +/- 20 K) however, using two different techniques to convert this data to absolute cross sections, report differences of 50%. DeMore et al. (1994) recommend the Wahner et al. (1987) absorption cross sections. These data have a reported accuracy of 3-5 %.

D.2.6.1 References

- DeMore, W.B., S.P. Sander, D.M. Golden, R.F. Hampson, M.J. Kurylo, C.J. Howard, A.R. Ravishankara, C.E. Kolb, M.J. Molina (1994), *Chemical Kinetics and Photochemical Data for Use in Stratospheric Modeling Evaluation Number 11*, JPL Publication 94-26
- Frost, G.J., L.M. Goss, & V. Vaida, (1996) "Measurements of High-Resolution Ultraviolet-Visible absorption Cross Sections at Stratospheric Temperatures: 2. Chlorine dioxide", *J. Geophys. Res.*, 101, 3879-3884.
- Wahner, A., G.S. Tyndall, & A.R. Ravishankara (1987) "Absorption cross sections for OClO as a function of temperature in the wavelength range 240-480 nm", *J. Phys. Chem.*, 91, 2734-2738.

Appendix E. Lunar Altitude Registration

The tangent height registration for the lunar radiometric measurements can be accomplished using a technique similar to the solar method described in the SAGE III Algorithm Theoretical Basis Document, Transmission Level 1B Products, Section 3.2.3. To accomplish the tangent height registration, the primary requirement is to accurately determine the position on the lunar limb, in angular units, of the measurement position. Meeting this requirement is complicated by the scanning motion of the instrument field of view over the target (moon), resulting in the radiometric measurements being taken at irregular points on the target limb, and the absence of accurate absolute pointing information from the instrument. Additionally, the instrument is designed to focus the scan plane through the radiometric center of the moon, which, unlike the case of the sun as the target, does not coincide with the geometric center of the moon. Information provided by the instrument used in the calculations to meet the limb position registration requirement includes the time of the radiometric measurement and the accurate relative pointing information derived from the movement of the instrument scan mirror. At each time increment, a detailed ephemeris calculation can be accomplished that solves the geometry data parameters for the spacecraft to Earth and moon. These ephemeris calculations provide the geometry position information from the spacecraft to the moon center, top, and bottom limbs.

To perform the tangent height registration, additional information will be required from a radiance model of the moon. Information required from the model includes the radiance center, terminator location, and rotation to the scan plane of the instrument. A radiance model is currently being developed as part of the NASA Earth Observing Spacecraft Mission by the U.S. Geological Survey and Northern Arizona University as Project ROLO. The radiance map of the moon, required as an input to the SAGE III model, could be the Project ROLO data when it becomes available, or some alternative to-be-determined source.

The tangent height computations are accomplished using the following steps:

1. A radiometric model predicts the radiometric center of the moon and establishes whether the upper or lower limb of the moon is inside the lunar terminator line.
2. The scan azimuth angle in angular units relative to the target is determined by the difference between the ephemeris calculated velocity to target angle and the measured relative azimuth change of the instrument.
3. An edge signature is established and used to accurately locate the first observation that falls on the top or bottom edge of the lunar disk. The edge signature is established using the second derivative inflection point as the edge crossing time.

4. A geometric height correction is calculated for the first observation based on the offset of the radiometric center of the moon from the geometric center of the moon, and the scan azimuth angle. The geometric height correction, in angular units, is applied to the first observation to correct for the height difference between the (known) height of the top (or bottom) of the lunar disk and the offset height of the first observation.
5. Relative scan mirror elevation movement is used to calculate the angular positions of the subsequent observation points on the lunar limb.
6. The refracted tangent altitude of each observation point is then computed from the angular positions using the same processing routine as the solar processing procedure.